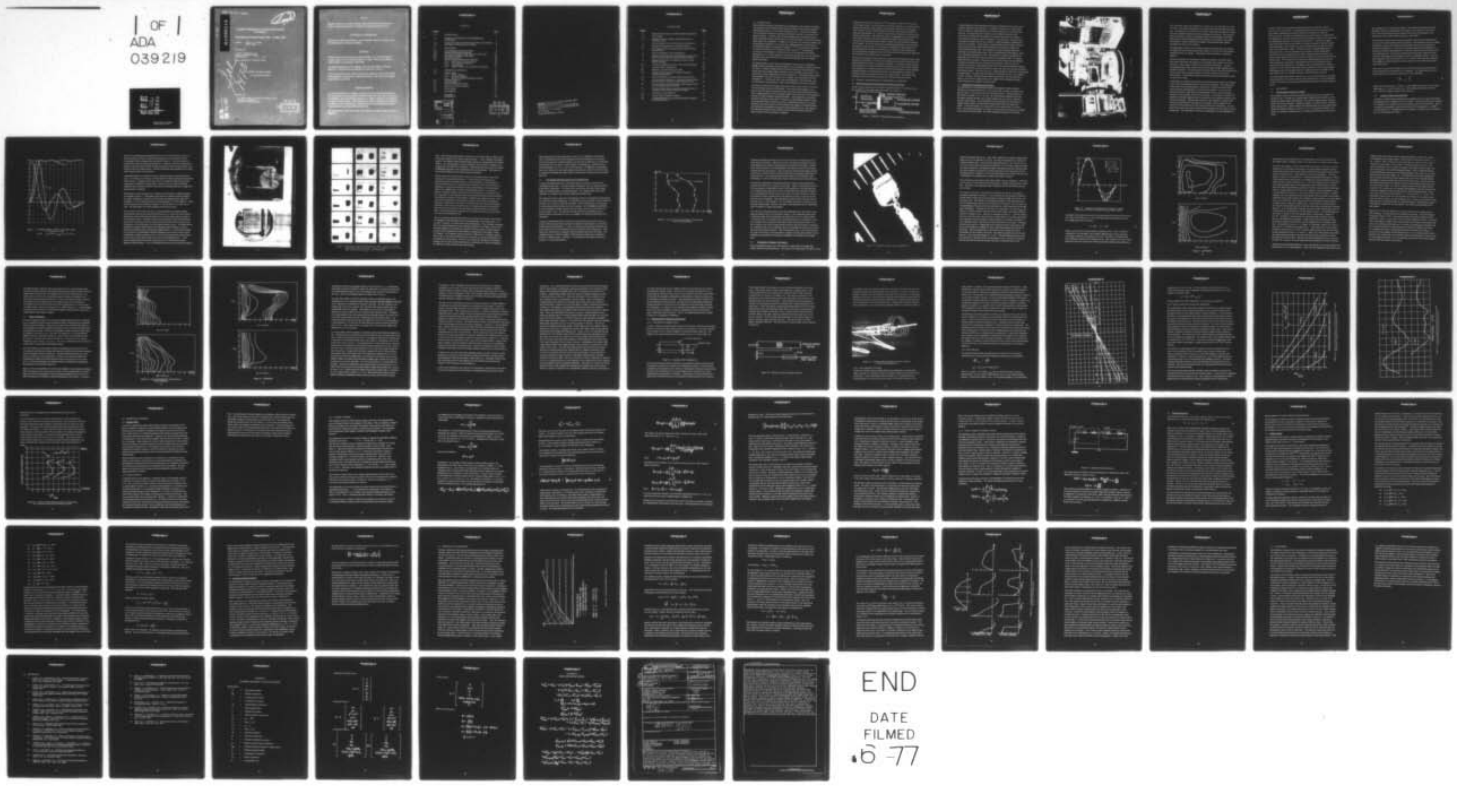
AD-A039 219 FAIRCHILD REPUBLIC CO FARMINGDALE N Y F/G 20/9
PLASMA ACCELERATION IN PULSED ABLATIVE ARC DISCHARGES.(U)
1977 D J PALUMBO, M BEGUN F44620-74-C-0055
UNCLASSIFIED AFOSR-TR-77-0623 NL

| OF |
ADA
039219



END

DATE
FILMED
6-77

AFOSR - TR - 77 - 0623

AD A039219

PLASMA ACCELERATION IN PULSED ABLATIVE ARC DISCHARGES

Final Report For Period 15 March 1974 - 31 March 1977

AUTHORS: DOMINIC J. PALUMBO
MARTIN BEGUN

PREPARED BY:

FAIRCHILD INDUSTRIES, INC.
FAIRCHILD REPUBLIC COMPANY
FARMINGDALE, N.Y. N.Y. 11735

UNDER CONTRACT NO. F44620-74-C-0055

APPROVED FOR PUBLIC RELEASE

DISTRIBUTION UNLIMITED

PREPARED FOR:

AIR FORCE OFFICE OF SCIENTIFIC RESEARCH (AFSC)
BOLLING AIR FORCE BASE
DISTRICT OF COLUMBIA 20332

AD No.
DDC FILE COPY

DDC
RECEIVED
MAY 10 1977
D

NOTICE

Qualified requestors may obtain additional copies from the Defense Documentation Center; all others should apply to the National Technical Information Service.

CONDITIONS OF REPRODUCTION

Reproduction, translating publication, use and disposal in whole or in part by or for the United States Government is permitted.

FOREWORD

This final report was prepared by Fairchild Industries, Inc., Fairchild Republic Company, under Air Force Contract F44620-74-C-0055, "Plasma Acceleration in Pulsed Ablative Arc Discharges", MS147V003.

The research reported upon was supported by the Air Force Office of Scientific Research. This program was monitored by Dr. Bernard T. Wolfson.

Work on this contract began in March 1974 and was completed by March 1977 and the pertinent studies of that period are reported upon herein. The report was submitted by the authors in April 1977.

ACKNOWLEDGMENTS

Our sincere gratitude to Dr. William J. Guman for his many fruitful informal discussions during the course of this effort, and without whom, this work could not have been accomplished. We are particularly grateful to Mr. William Johnson for his assistance in setting up the test facility and his contributions in the area of high speed photography. Our thanks are also extended to Mr. John Muldoon for his help in setting up the high voltage electronics and running the diagnostic tests.

This technical report has been reviewed and is approved for public release; distribution unlimited.

CONTENTS

Section		Page
1.0	INTRODUCTION	1
2.0	PHYSICAL BACKGROUND AND EXPERIMENTAL APPARATUS	2
2.1	General Description of Pulsed Ablative Plasma Accelerators	2
2.2	Description of Laboratory Test Facility	3
3.0	DIAGNOSTICS	6
3.1	Total Discharge Current and Voltage	6
3.2	Results of High Speed Photography	7
3.3	Arc Velocity and Shape Using Time-of-Arrival Probe	13
3.4	Distribution of Magnetic Flux Density	15
3.5	Current Distribution	23
3.6	Electron Number Density and Temperature	29
	3.6.1 Description of Langmuir Probe	29
	3.6.2 Data Acquisition Procedure	31
	3.6.3 Data Reduction	32
	3.6.4 Number Density and Temperature Distribution	34
4.0	THEORETICAL APPROACH	38
4.1	Physical Model	38
	4.1.1 Initial Conditions	38
	4.1.2 Boundary Conditions	40
	4.1.3 Plasma Coupling to Discharge Circuitry	46
4.2	Governing Equations	48
4.3	Chemical Model	49
4.4	Numerical Integration Scheme	53
5.0	RESULTS OF CALCULATIONS	55
6.0	CONCLUSIONS	63
7.0	REFERENCES	65
	APPENDIX A	67
	APPENDIX B	70

ACCESSION for
NTIS White Section
DDC Buff Section
UNANNOUNCED
JUSTIFICATION
BY
DISTRIBUTION/AVAILABILITY CODES
Dist. AVAIL. and/or SPECIAL
A

DDC
RECEIVED
MAY 10 1977
D

AIR FORCE OFFICE OF SCIENTIFIC RESEARCH (AFSC)
NOTICE OF TRANSMITTAL TO DDC
This technical report has been reviewed and is
approved for public release IAW AFR 190-12 (7b).
Distribution is unlimited.
A. D. BLOSE
Technical Information Officer

ILLUSTRATIONS

Figure		Page
1.	Schematic Cross-Section of Pulsed Ablative Accelerator	2
2.	Test Facility	4
3.	Discharge Current, Voltage, and Energy Input as a Function of Time	8
4.	Mirror Images of Front and Side Views of Accelerator	10
5.	High Speed Photographs of Accelerating Plasma	11
6.	Arc Front Location and Shape Obtained Using Time-of-Arrival Probe	14
7.	Small Coil Magnetic Probe Magnified 20X	16
8.	Magnetic Probe Response and Discharge Current Versus Time at Various Positions Along the Ablator Surface	18
9.	Magnetic Flux Density Distribution at Various Times During Discharge	19
10.	Current Distribution at Various Times During Discharge	24
11.	Langmuir Probe Configuration	29
12.	Schematic of Probe Cleaning Circuitry	30
13.	Langmuir Probe Equipped for Remote Cleaning by Electron Bombardment	31
14.	Typical Volt-Ampere Langmuir Probe Characteristic	33
15.	Electron Number Density as a Function of Distance Along the Accelerator Centerline at Three Different Times	35
16.	Typical Langmuir Probe Response and Discharge Current 2cm Past the Electrode Exit Plane	36
17.	Electron Number Density Across the Interelectrode Gap a Distance 2cm Past the Electrode Exit Plane	37
18.	Equivalent Circuit Schematic	47
19.	Typical Wave Propagation Diagram	56
20.	Computed Magnetic Flux and Current Density During the First Quarter Cycle	60

1.0 INTRODUCTION

Spacecraft and associated communications, photographic, and computer technology have reached a level of sophistication requiring attitude control systems capable of maintaining fractions of an arc second pointing accuracy. Among the candidates for the auxiliary propulsion subsystem are hydrazine, cold gas, electrostatic and plasma thrusters. Of these, only the pulsed ablative plasma accelerator offers highly repeatable discrete impulse bits of microsecond duration as well as equivalent steady state thrust capability. In addition to this feature, the intrinsic simplicity and corresponding reliability of this concept have inspired satellite manufacturers to develop flight qualified microthruster hardware, [1,2,3,4] and government agencies to continue development of a millipound thruster system. [5,6,7] Although this current area of development is the primary one, other applications for plasma accelerators, i.e.; isotope separators, simulators and injectors, have all prompted this basic study into the dynamics of the plasma acceleration process in pulsed ablative discharges.

To the present day, no truly basic understanding of the processes of propellant ablation, plasma production, energy transfer to, and acceleration of plasma exists for this device. Sufficient empirical data correlations which have been generated in past years have enabled design of thrusters to meet specific requirements, [8] but none of these include optimization of thruster efficiency. It is believed that if a good understanding of the basic processes were available, such optimization could be accomplished. Furthermore, other associated application oriented details, such as exhaust plume characteristics, could be extrapolated and, perhaps, predicted.

Previous investigations into pulsed acceleration of plasma have all been concerned with accelerating a gaseous working fluid. At the onset of this program it was presumed that the basic processes associated with accelerating a plasma produced from a subliming ablator were considerably different than those in the case of gaseous injection or static breakdown induced discharges. This supposition was justified during the first phase of this effort, [9] wherein a one-dimensional continuum model was formulated using the unsteady equations of magnetohydrodynamics as a basis. Obtaining a numerical solution to those equations was plagued by stability problems and a peculiar non uniqueness associated with the initial time step. Nevertheless, the experimental data and some analytic work with MHD equations had led to a clearer picture of the acceleration mechanism.

During the second phase of this effort,[10] measurements made in the first phase were extended to give a two-dimensional picture of the plasma as a function of time. Magnetic flux density, local average current density, and time of arrival probes were utilized in order to measure some of the more salient plasma parameters. High speed photography (i.e., 2M fps) was also used to determine the motion of the luminous plasma front. The diagnostic study was augmented by a two-species continuum MHD model in which the one-dimensional model of the first phase was extended to two-dimensions and the effects of finite viscosity and heat conductivity were included. At the end of that phase computational difficulties were still being encountered but the reasons for occurrence of instabilities in the numerics were becoming apparent and steps were being taken to circumvent these instabilities. The two-dimensional diagnostics were very successful and yielded further qualitative understanding of the ablative plasma accelerator.

The third and final phase of this program was geared toward obtaining a better understanding of the chemistry involved in producing plasma by depolymerization of solid tetrafluoroethylene (Teflon, as produced by DuPont). This study included Langmuir probe measurements of the two-dimensional distribution of electron number density and temperature, a detailed evaluation of chemical and ionization reactions possible among the products of depolymerized Teflon, and incorporation of a finate rate ionization reaction and neutral species in the analytic model. The results of this final phase and of the previous two phases are included in this final report.

2.0 PHYSICAL BACKGROUND AND EXPERIMENTAL APPARATUS

2.1 General Description of Pulsed Ablative Plasma Accelerators

Energy storage capacitors are connected in parallel through a low inductance strip line assembly to two parallel planar electrodes (see Figure 1).

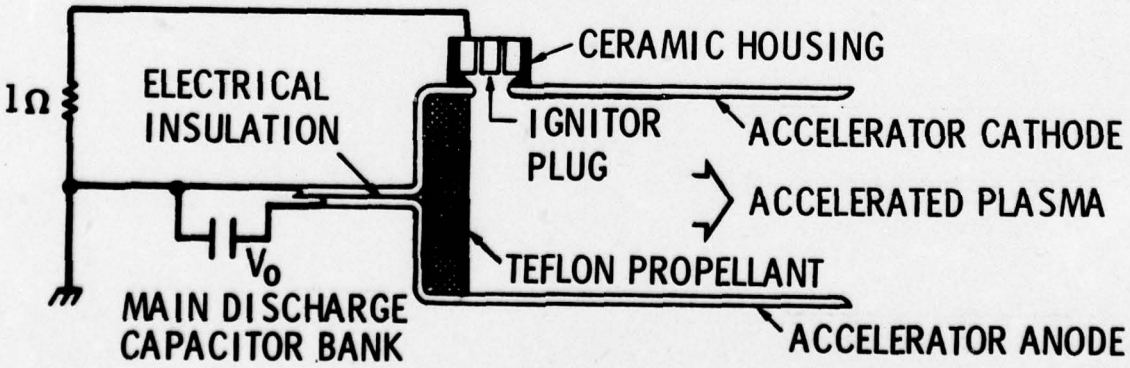


Figure 1. Schematic of Pulsed Plasma Accelerator

A solid propellant (Teflon) is positioned between the electrodes at the same end at which the strip lines are connected. The cathode is fitted with an "igniter plug" which consists of a cylindrical anode and cathode separated by a semiconducting material. The dimensions of this plug are much smaller than those of the accelerator electrodes and the cathode of the plug is connected to the cathode of the accelerator through one ohm of resistance. The accelerator is fired by first charging the capacitor bank to some voltage V_o which will appear simultaneously across the electrodes. The presence of vacuum between the electrodes, however, allows retention of this charge without breakdown with the usual voltages and interelectrode spacings used. The capacitors are then discharged through the electrodes by firing the ignitor plug. This is accomplished by discharging a separate 2 microfarad capacitor from 600 VDC through a 1:3 step-up transformer by triggering an SCR in series with this capacitor on the primary side. The ignitor plug, when fired, produces a miniscule amount of ionized matter having sufficient conductivity to break down the accelerator electrode gap. Since the one ohm resistance represents a high impedance path, the main capacitor discharge initiates between the accelerator anode and cathode, rather than returning to ground through the ignitor plug cathode. Some time later (i.e., appromimately 50-200 ns) the Teflon begins to depolymerize, a process which transforms the solid directly into a gas composed of heavy molecules. Subsequent dissociation and ionization of this gas produces a plasma, into which the energy stored in the capacitor bank is deposited through Joule heating and the creation of magnetic field.

2.2 Description of Laboratory Test Facility

The accelerator and vacuum pumping station were designed to allow maximum flexibility and instrumentation ease. The vacuum station consists of a glass T-jar placed on top of a 4-inch (10.16 cm) diameter pump system. Ultimate pressure in this facility is roughly 2×10^{-5} mm Hg. The main discharge capacitor bank and discharge initiating circuitry were located outside of the jar to yield a maximum amount of space inside. The accelerator electrode assembly was connected to the capacitor bank through two coaxial feed-throughs fabricated from oxygen-free copper. Electrodes measure 4.0 inches (10.16 cm) in width and are 4.0 inches long. The interelectrode gap is 3.0 inches (7.62 cm) and the electrodes are parallel to each other over their length. The Teflon propellant consists of a 0.313 inch

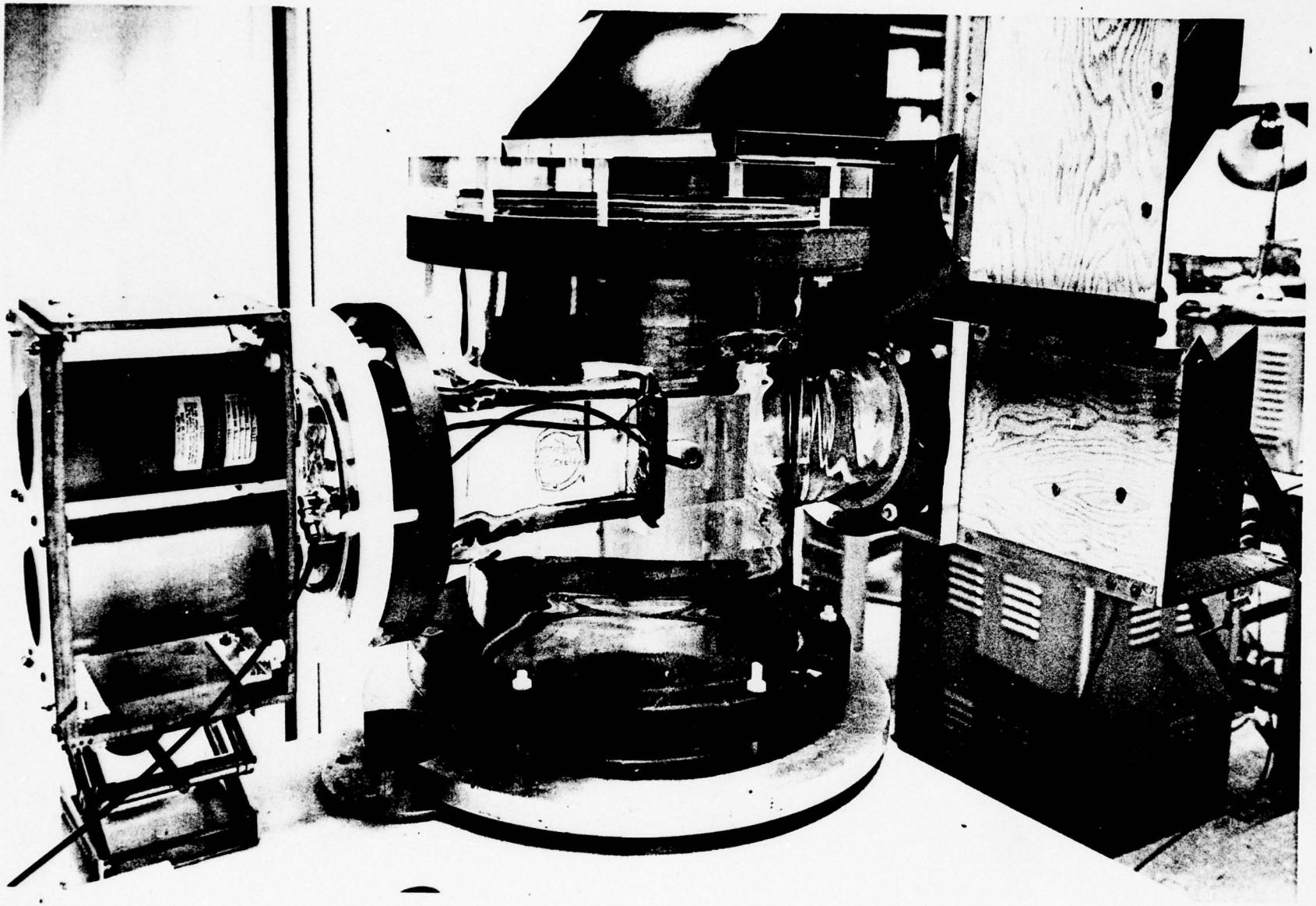


Figure 2. Test Facility

(7.95 mm) thick slab having a height of 2.9 inches (7.37 cm) and width of 1.0 inch (2.54 cm). This slab is positioned at the center of the electrode width at the back end. Two pieces of 0.25 inch (6.35 mm) Mykroy 1100 ceramic are placed on either side of the propellant slab to shield the remaining electrode area. The excessive electrode width (as compared to propellant width) was incorporated to eliminate fringe effects of the electromagnetic fields between the electrodes in the vicinity of the plasma, thereby making the assumption of two dimensionality implied throughout this study more consistent.

The ignitor plug is located in an insulated housing immediately above the cathode. The plug fires into the interelectrode gap through a 0.25 inch (6.35 mm) diameter chamfered hole in the cathode. A photograph of the test facility is included in Figure 2.

In order to facilitate two dimensional scanning of the plasma, all probes which were used in this study were fastened to an assembly which could be moved from outside the vacuum station in both the axial and latteral directions. This was accomplished using rotary motion vacuum feed throughs, flexible shafting and two Unislide assemblies. This arrangement allowed a complete scan of the interelectrode gap to be made with each probe without ever having to break the vacuum for repositioning. It also allowed extremely accurate positioning of the probes relative to a fixed known origin.

A high degree of resolution was desired so as to determine the space/time evolution of the measured plasma parameters as accurately as possible. This requirement implies that the interelectrode gap be scanned over a relatively fine grid which means that many individual pieces of data would be obtained. Use of a normal analog oscilloscope would require taking photographs of the events at each probe location and later reducing this data by measuring, as accurately as possible, the amplitude of recorded signal and its time relative to some consistent reference time during the discharge. This procedure would have been expensive considering the cost of film and would also have required an excessive man hour effort for the reduction of data because of the large amount of data to be accumulated. For this reason the decision was made at a point during the program to rent a digital memory oscilloscope. The advantages of this kind of oscilloscope over the analog type are

two fold. Data is received and automatically converted to numerical values in volts via an A to D converter. The analog signal is sampled at a preset interval of time between samplings and the data is stored in numerical form within the built-in memory. The data is also displayed in the form of dots on a screen which are separated by the preset time interval, and this display remains on the screen until it is deliberately erased by a new signal or by the user. To retrieve the digital value of the signal at any of these points it is merely necessary to call out the point in question using a cursor which moves from one point to the next and read off its value in volts (accurate to within $\pm$ 1%) directly from the digital display which is also on the screen. The two advantages are, therefore, that no photographic record of the event is required since the data is obtained directly from the scope and no lengthy expendure of time is necessary to generate the numerical data from an analog record. The savings in cost of film alone defrayed approximately half the cost of renting the scope which is manufactured by NICOLET Instrument Corp. (Model 1090A with 93A plug-in). The digital memory oscilloscope has a frequency response of 1 MHz which is sufficiently high to record the events measured during this program since the discharge cycle has a ringing frequency of roughly 16 kHz. Other plug-in units are available which have 10 MHz frequency response.

Use of the digital scope allowed scanning over a much finer grid than was originally anticipated because of the large savings in data reduction time, and has contributed to the overall success of the experimental effort and accuracy of the data presented herein.

3.0 DIAGNOSTICS

3.1 Total Discharge Current and Voltage

The discharge current and voltage across the electrode gap were measured as a function of time. Current was measured using a Rogowski Coil wound so as to fit around the cathode behind the propellant. The coil was calibrated using a precalibrated coil of known accuracy. Discharge voltage was measured using a Tektronix 1000:1 voltage probe. Initial voltage on the capacitor bank was set precisely using a digital DC voltmeter having an accuracy of $\pm$ .1%. The current and voltage waveforms were displayed simultaneously on a Tektronix Model 555 dual beam oscilloscope.

The oscillograms are reproduced in Figure 3 where discharge current and voltage throughout the first 13 microseconds of the discharge are plotted as a function of time. The energy delivered by the capacitor bank, given as the integral of the instantaneous power (current times voltage), is also plotted.

The current and voltage curves deviate considerably from what one would expect to see in an LRC circuit with fixed discrete elements. The deviations are due to coupling of the plasma motion via the induced magnetic fields and the time variant plasma resistance and inductance. The degree of deviation suggests strong coupling; i.e., the plasma resistance and inductance are much larger than those of the fixed portion of the discharge path. The fact that virtually all of the energy is delivered by the capacitor during roughly the first quarter cycle is of particular interest. Also note that subsequent cycles only transfer from 2 to 2.5J back and forth to the capacitors. The significance of this observation becomes clearer as more information appears later in this report.

Fairly good energy delivery efficiency (93.1%) from the capacitor bank indicates a time-averaged ESR of approximately 2.9 milliohms. The initial inductance at the instant breakdown occurs can be estimated from the relationship

$$\left(\frac{dI}{dt}\right)_{t=o} = \frac{V_o}{L_o} \qquad (1)$$

Where I is the total current, t is time, V_o is the initial voltage, and L_o is the initial inductance (i.e., of the circuit plus arc). The oscillograms indicate a dI/dt of 2.6×10^{10} A/s, yielding a value of 115.6 nH for L_o.

3.2 Results of High Speed Photography

A Beckman & Whitley Model 189 High Speed Framing Camera was used to photograph the discharge from its initiation to near completion. This camera will take a maximum of 25 exposures at a maximum rate of one exposure every 0.4 microseconds. Since it was desired to photograph at least the first cycle of the discharge (i.e., roughly 7 microseconds) with a meaningful degree of resolution, a framing rate of one exposure per 0.5 microseconds was chosen.

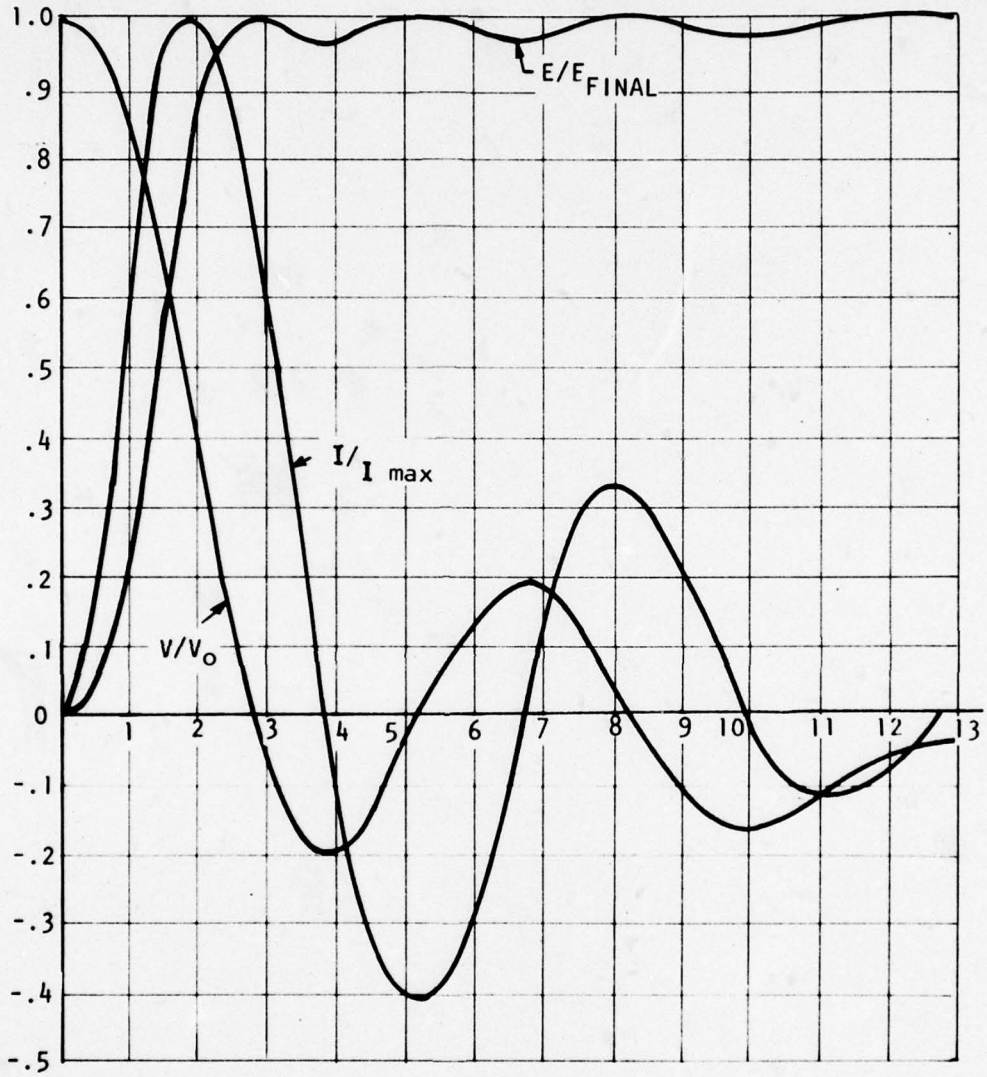


Figure 3. DISCHARGE CURRENT, VOLTAGE, AND ENERGY INPUT AS A FUNCTION OF TIME

V_o=3kV I_{max}=29.9kA E_{FINAL}=76.3J E_o=81.9J

The arc was simultaneously photographed from the side and front using a system of four front surface mirrors to project both images side by side at the same level. A photograph of this arrangement is presented in Figure 4. The camera lens was located some 25 feet (7.62m) from the mirrors. A front view of the arc evolution was desired so that the relative lateral velocity of the plasma could be determined for comparison to its forward progression. With this information the assumption of two dimensional motion could be cross-checked.

Considerable effort was required in order to initiate framing at the instant of breakdown. To do this it was necessary to fire the thruster using the output signal generated by the camera. In addition, the thruster had to be completely isolated from ground subsequent to charging the capacitor bank. Several runs were made in which the angular location of top-dead-center in the camera was adjusted until only a single frame appeared prior to initiation.

Photography was done without the use of filters ahead of the lens. A typical sequence is presented in Figure 5. Photographs of the front view indicate that the arc begins as a fairly straight line centered on the electrodes and against the face of the Teflon propellant. At 0.5 μs the line appears to be approximately 1.7 cm in width and uniform. A half microsecond later the line is roughly 3.2 cm wide and at 1.5 μs it is 3.4 cm wide. The width appears to remain constant past that point in time.

The view from the side shows that the arc remains against the propellant surface as the luminous front moves forward up until about 2.5 μs where a thin dark region is visible between the initial luminous plasma and a second luminous plasma present at the propellant surface. Note that at this time the first quarter cycle of the discharge current has not yet ended, but peak current has been reached and the current is now decreasing. As time progresses, the dark region increases in size. The initial plasma continues its forward motion and the second luminous region continues to remain against the propellant surface and becomes slightly thicker. At zero current (roughly 3.9 μs) there is no discernible irregularity introduced and the above events proceed continuously up until the exposure at 5 μs, where the second luminous region appears to have moved off the ablator surface and move forward behind the first. A dark region is again evident between this second plasma and a third luminous region against the Teflon surface. At 5 μs the discharge current has just reached its negative

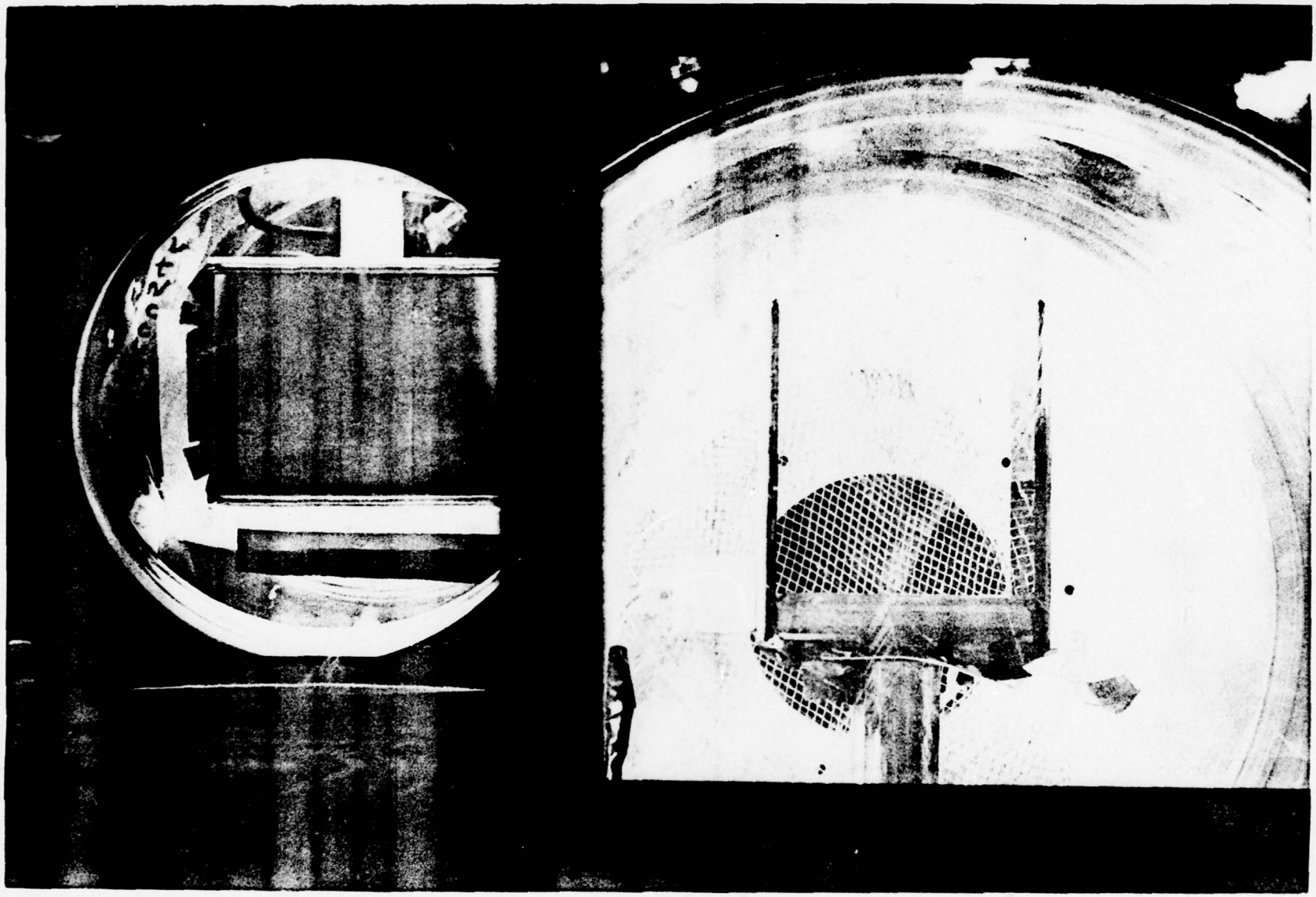


Figure 4. Mirror Images of Front (Left) and Side (Right) Views of Accelerator

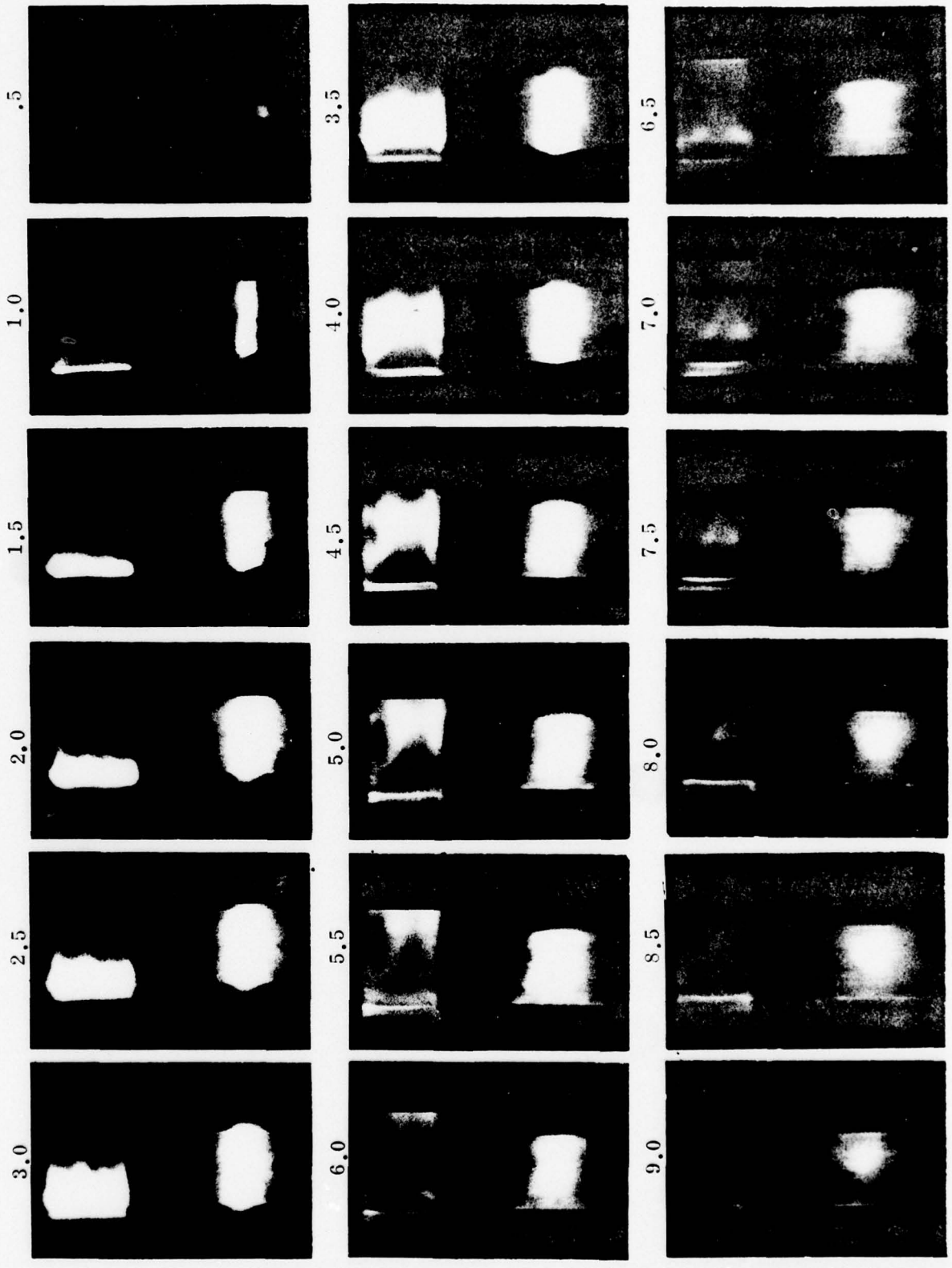


Figure 5. Simultaneous High Speed Photographs of Side & Front of Accelerator - Side View on Left, Anode Left - Front View on Right - Anode Bottom. Time in Microseconds at Left of Each Photograph.

peak. The second luminous plasma continues to move forward while the third appears to remain in position at the surface of the propellant. A close scrutinty of the photograph at 8 μs indicates that the third luminous plasma has separated from the ablator surface. The second positive maximum discharge current occurs at roughly 7.8 μs or just prior to the third arc's separation. Beyond this point in time the arc becomes insufficiently luminous to draw conclusions from the photographs. The images are not as clearly defined and are barely evident when printed.

Certain conclusions concerning the evolution of accelerated plasma can be drawn from the above experimental evidence. It is first obvious that the plasma is accelerated in discrete bunches which are called plasmoids. The appearance of these plasmoids seems to be coincident with each quarter cycle of the current and, furthermore, each plasmoid appears to begin accelerating away from the ablator surface at or slightly after a maxima of the discharge current. It was shown, however, through an analytic treatment of the one dimensional arc dynamics, that the "separation" of each plasmoid off the ablation surface actually becomes incipient at the instant the direction of the gradient of magnetic flux density reverses. This reversal in the gradient of B at the ablator surface is the result of the change in direction of current flow at the ablator, which leads the reversal of total discharge current by a small amount of time because of the inductance between the capacitor bank terminals and the point on the electrodes at which the ablator is positioned. Thus, each plasmoid begins to separate from the ablator surface just prior to each reversal of the discharge current.

There is no apparent discontinuity in the plasma motion at the current reversal times even though the total discharge current is instantaneously zero at these times. No so-called "restrikes" are obvious from these photographs. This, and other supporting data, led to the hypothesis that each subsequent plasmoid is in reality a portion of the previous standing arc which has been "sheared" off by the action of strong magnetic pressure forces generated once the direction of current flow at the ablator surface has changed. The continuous depolymerization of Teflon allows a sufficient quantity of new mass to enter the interelectrode gap to keep the arc sustained through the zero total discharge current points. Moreover, the current flow through each subsequent standing arc is in part also flowing through the accelerating arc, thereby coupling the two while they coexist within the interelectrode gap.

With regard to the two dimensional shape of the arc, it is difficult to ascertain the true arc configuration from these photographs since the luminosity is very intense. The arc does appear to be fairuly uniform across the gap up until about 3 microseconds but beyond that one can detect a certain degree of nonuniformity, especially obvious in the photographs at 4.5, 5.0, and 5.5 microseconds. The difficulty in interpreting the true arc shape from these photographs prompted the use of time of arrival probing to determine the leading edge shape and the result of these measurements are reported upon next.

3.3 Arc Velocity and Shape Using Time-of-Arrival Probe

A double electrostatic probe was constructed using 0.125 inch (3.2 mm) diameter semi-rigid coaxial cable. The outer and inner conductors were the cathode and anode of the probe; respectively. A 9V battery was used to drive the probe and the output signal was detected using a current transformer. The outside surface of the outer conductor was insulated with a coating of high temperature epoxy.

The current tansformer output and total discharge current were displayed simultaneously on a dual beam analog oscilloscope. The discharge current provided a common reference for time zero, needed to do the data reduction. Several oscillograms were recorded at each location probed and these data were averaged. Due to significant uncertainty, it was not possible to decifer accurate time-of-arrival any closer to the ablator surface than about 3.5 cm. The maximum distance allowed by the facility from the ablator surface to the probe was 12 cm, or roughly 3 cm beyond the exit plane of the electrodes.

In order to determine the shape of the front at given times the raw data on time-of-arrival of the first plasmoid was plotted as a function of axial distance at each lateral position between the electrodes. A curve was then drawn through the data points and the position of the front at the desired time was read from each of these plots. These points were then plotted as a function of lateral position between the electrodes. The resulting curves are plotted in Figure 6 which shows the shape of the accelerating front at two different times. The line $x = o$ corresponds to the ablator surface and the line $y = o$ is the anode surface.

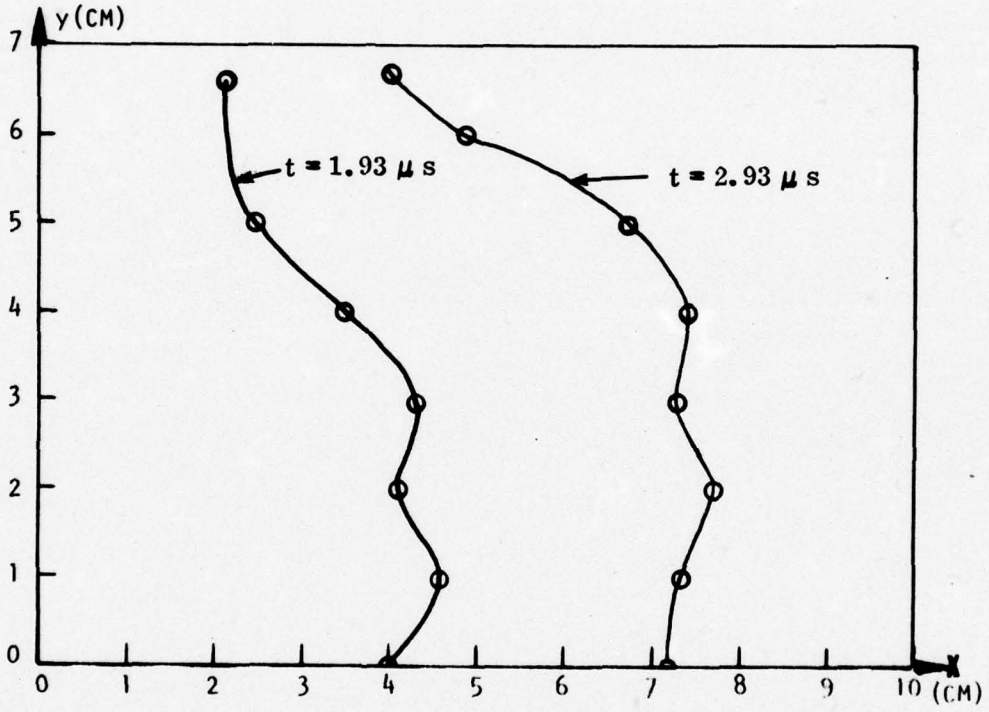


Figure 6. Arc Front Location and Shape Obtained Using Time-of-Arrival Probe

The first conclusion drawn from the data is that the front is moving faster at the anode than at the cathode. Indeed, the raw time-of-arrival data indicates that the front velocity at the cathode is approximately one-half that at the anode. Furthermore, the front appears to be fairly uniform over between 50 and 75% of the interelectrode gap from the anode up. The raw data also shows that the uniform portion of the front is moving at fairly constant velocity after accelerating during approximately the first 1.5 microseconds and that the velocity near the cathode, while increasing up to about 2 microseconds, begins to slowly decrease beyond this time.

No conclusive information concerning the second or other subsequent plasmoids could be drawn from the raw time-of-arrival data. While a second discrete peak in the output signal was discernible in some of the oscillograms, this peak appeared to be merged with the first in some cases and appeared to be nonexistent in others. It was not understood why this was the case, but it was presumed that it was due to the statistical nature of such probes in detecting the presence of a plasma via the presence of its conductivity. This explanation seemed plausible since the shape of the peaks even at a given position were not identical from shot-to-shot but, on the contrary, differed quite a bit from each other, even though the onset of current flow (time of arrival) was fairly reproducible.

One of the more interesting observations concerning this data is the absence of any apparent boundary layer at the electrode surfaces. Even though the closest point at which the probe could be positioned to the electrodes was 3 mm off the surface, at a distance of 10 cm downstream from the ablator surface one would expect to see some boundary layer structure at this distance above the electrode surface. One fact is certain on the basis of front location and that is that the presence of viscosity in a continuum sense is not a significant factor in controlling the motion of the plasma front near the electrode surfaces. This is probably the case, at least with regard to the motion of the front, because the plasma density at the front is low and the no-slip condition at the electrodes is probably not applicable in the vicinity of the leading edge.

3.4 Distribution of Magnetic Flux Density

Small coil magnetic probes were constructed for measurement of magnetic flux density within the interelectrode gap. The probes were wound using .008 inch (0.2 mm)

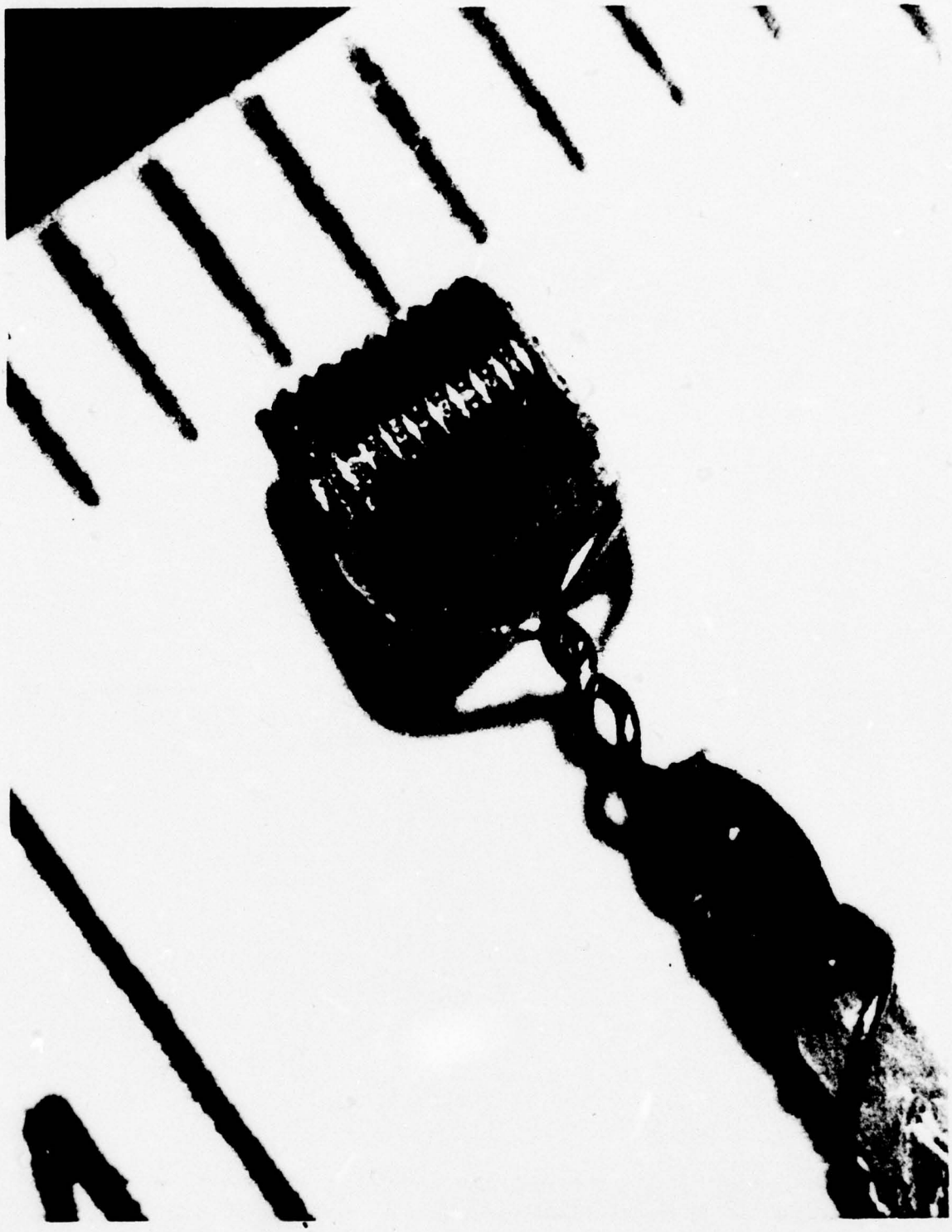


Figure 7. Small Coil Magnetic Probe Magnified 20X

diameter lacquered copper wire. Each probe consisted of 9 complete closely spaced turns on an I. D. of .069 inch (1.75 mm). The ends of the probes were soldered to miniature coaxial cable. Dense alumina tubing having anO. D. of 6 mm and I. D. of 3 mm was used to house the probe and coaxial line. The end of the tubing containing the probe was potted to a hemispherical shape with high temperature resistant epoxy. The epoxy potting was necessary to protect the probe from the hot plasma and was advantageous since it allowed a more streamlined shape to be molded at the tube end. A photograph of a magnified probe winding is presented in Figure 7.

Data were taken on the Nicolet Model 1090A digital memory oscilloscope. The probe was moved in .25 cm increments in both directions, yielding excellent spatial resolution. The probes were calibrated using a Helmholtz coil and showed flat response up to 10 MHz.

In our first year's work, measurements of magnetic flux density only along the accelerator centerline were made. It was seen there that the temporal variation of B at the ablator surface followed the discharge current to within a few percent over the entire cycle. The analytic one-dimensional prediction of the appropriate constant of proportionality between B and i indicated an arc width of 2.93 cm which was in surprisingly good agreement with the luminous arc width measured off of the high speed photographs. Following up with this in two dimensions, the ratios i/i_{max} and B/B_{max} at various locations along the surface of the ablator were plotted simultaneously as a function of time. This plot is presented in Figure 8. The first observation to be made from these data is that the magnetic flux is very nearly proportional to the discharge current everywhere along the surface of the ablator, but there is some distinction between the first and second half cycles of the current. During the first half cycle there is a slight gradient in B along the surface of the ablator such that B is increasing from roughly the center of the interelectrode gap towards the electrodes. The second half cycle is characterized by a gradient in B with B decreasing from the cathode to the anode. The minimum negative value of B at the anode is -0.50T and at the cathode it is -0.81T. The slight gradient evident in the first half-cycle is within the realm of experimental error, but there is no question about the fact that the observed gradient during the second half cycle is real.

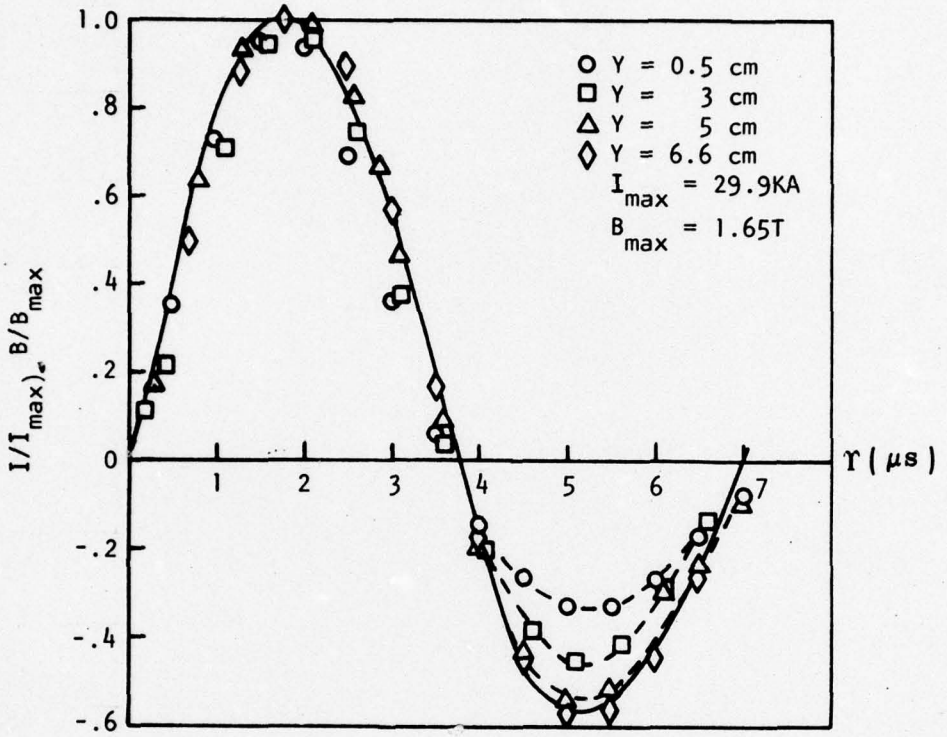
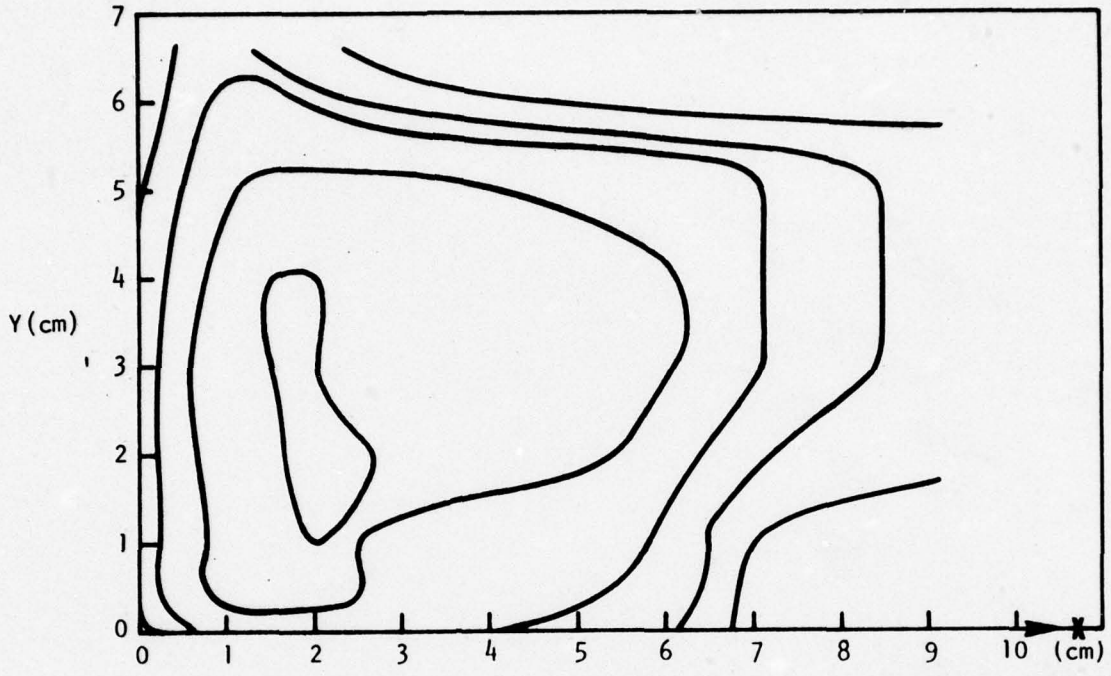


Figure 8. Magnetic Probe Response and Discharge Current versus Time at Various Positions Along the Ablator Surface

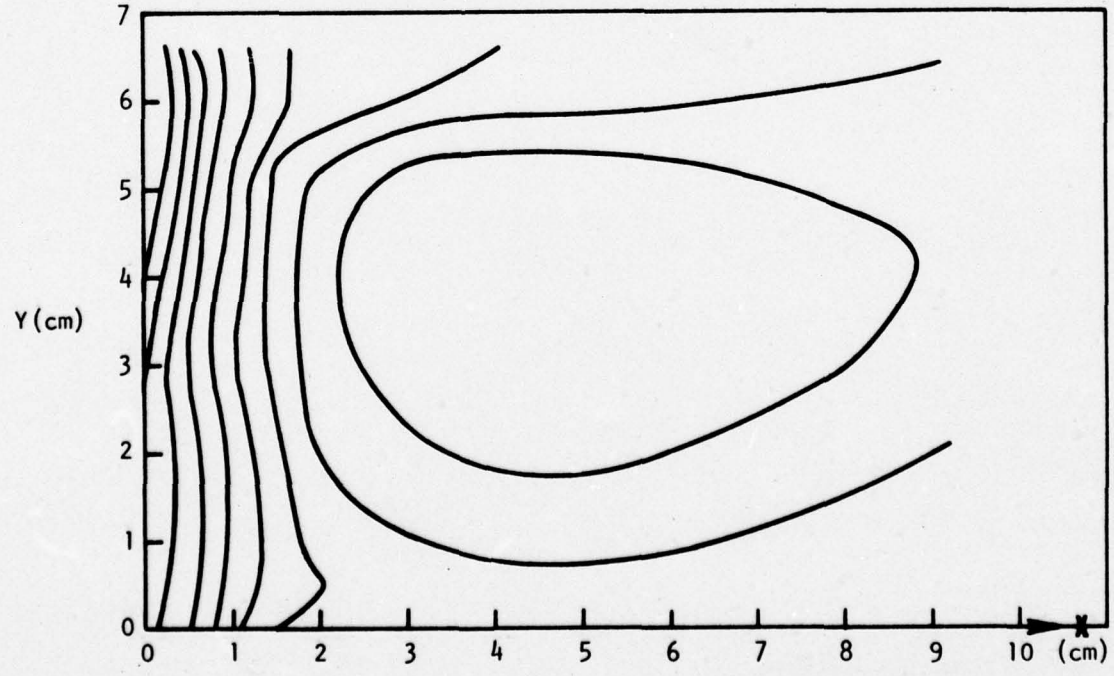
A gradient in the direction indicated would imply a finite flow of current away from the surface of the ablator (i.e., in the axial direction) as indicated by Amperes law in differential form which gives

$$J_1 = B_y/\mu \qquad J_2 = -B_x/\mu \tag{2}$$

where J_1 and J_2 are the current density components in the x- and y- directions; respectively, and subscripts x and y indicate differentiation in those directions. A curvature in the lines of current flow away from the ablator is dictated by the above equations and the observed direction of B_y. This curvature was more or less expected to exist once the time-of-arrival data had been obtained since those data



(c) t = 3.85 μs



(d) t = 4.85 μs

Figure 9. (Continued)

showed that the acceleration front was moving faster at the anode surface than at the cathode surface, implying a thicker arc at the anode as compared to the cathode.

The above observations are more clearly indicated in Figure 9 where the magnetic flux lines have been plotted at four stages of arc progression during the discharge. The first plot (Figure 9a) shows the lines of constant B at the instant of peak current in the first half-cycle (i.e., approximately 1.93 μ s from initiation). The lines begin at a value of 1.15T closest to x = o and the increment between lines is -0.165T. At this instant of time the presence of a standing arc is clearly evident from the very rapid decrease of B from the value at x = o. It is also obvious that the y-component of the current density (J_2) is considerably larger at the cathode than at the anode. Numerical differencing indicates a gradient of .53T/cm near the ablator which translates to a current density of 42 MA/m^2 at the cathode. Similar calculations reveal a current density of 25 MA/m^2 at the anode surface close to the ablator. Further analysis of the data indicates that the current density is fairly constant at the surface of both the anode and the cathode out to a distance of approximately 1 cm at the cathode and 2.8 cm at the anode, after which the current density falls off rapidly until the B- field reaches its minimum negative value. At that point the current density is zero and one would suspect that this would define the maximum downstream extremity of the arc. It is seen that this is truly the case once the data obtained using time-of-arrival probes is superimposed on the flux density contours. The leading edge position shown in Figure 6 has been superimposed as a dotted line on Figures 9a and 9b. In Figure 9b the flux lines one microsecond after maximum current (2.93 μ s after initiation) are plotted. At this instant of time the high speed photographs do not indicate arc separation and this is supported by the magnetic probe data. The flux line closest to x = o in Figure 9b represents a field of .99T with an increment of -.165T between subsequent lines. At this instant the cathode current density has decreased to 4.5 MA/m^2 near the ablator and the anode current density has also decreased in value to .67 MA/m^2. Again, the current density at the anode and cathode surfaces appears to be fairly constant up until a downstream distance just short of the plasma front. Skewing of the current density lines is more obvious in Figure 9b, however, as can be interpreted from gradients of B in the y-direction.

Perhaps the most interesting flux plot occurs at the instant of zero current (Figure 9c) which occurs 3.85 μ s after initiation. At that time the magnetic flux still shows small

positive values at the ablator surface which range between .07T and .2T, but the axial gradient of B has changed sign. The line closest to the ablator surface (x = o) has a value of .083T and the increment between lines is .083T up to the central closed loop representing .413T, and then -.083T beyond that closed loop. The observed change in B_x from positive to negative at the ablator surface implies that the current density at the wall has changed direction. This is of interest because the total discharge current has not yet changed direction and, in fact, is zero at the instant of time depicted in Figure 9c. No conclusions can be made regarding the flow of current in the plasma at this instant solely on the basis of the flux density distribution, but the measurements of local current flow using a current probe has shed considerable light on the situation and those results appear in the next section. It is obvious from Figure 9c, however, that separation of the first plasmoid has occurred. This is clear from the magnetic flux distribution since the absolute value of the axial gradient of B has two local maxima within the plotted demain. These two maxima are located in the intervals $0 < x < 1$ cm and $6 \text{ cm} < x < 8.5$ cm. The appearance of these maxima in $|B_x|$ manifest the existance of two separate arcs; one at the ablator surface, and one downstream of it. Moreover, the relatively large value of B_y near the cathode surface in particular indicates considerable curvature in the lines of current flow near the cathode. More will be said about this in the next section.

Figure 9d is a plot of the flux lines one microsecond after zero current (4.85 μ s after initiation). The line closest to the ablator has the value -.495T and the increment between lines is .083T. The current density at the ablator surface near the cathode has a value of -28.4 MA/m^2 and at the anode surface the value is -10 MA/m^2. Thus, the existence of higher local current density at the cathode as compared to the anode, noted during the first half cycle, is also the case during the second half cycle. The large axial gradient in B which extends from the ablator surface out to about 1.8 cm defines the extent of the second plasmoid at the instant of time shown. A second local large gradient of B downstream from x = o is no longer present at this instant of time, which leads one to conclude that the first plasmoid has already moved out of the interelectrode gap. To what extent this observation is true will be further analyzed in the next section of this report.

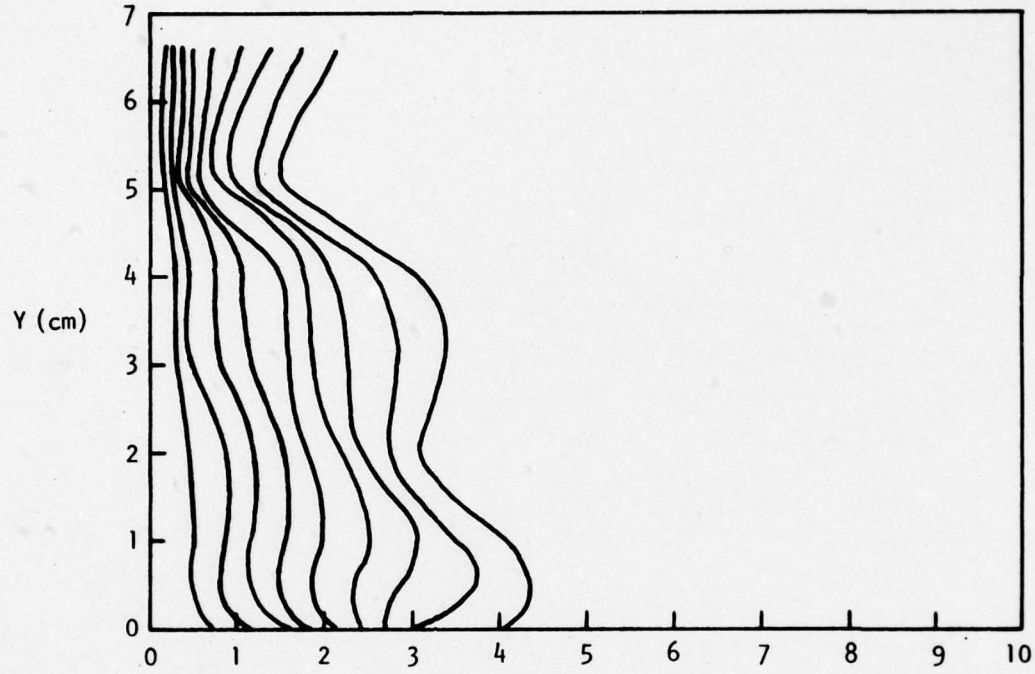
No further analysis of the data will be made beyond 4.85 μs of the discharge cycle, the reason for this being that a reasonably accurate interpretation of the data becomes difficult after this time due to the relatively low level of the measurements. It is noted, however, that the most interesting aspects of plasma acceleration in this device have already occurred by this time. Namely, the initial generation of plasma; the separation of the standing arc from the ablator surface and its subsequent acceleration out of the interelectrode gap; and the regeneration of a second standing arc which coexists with the accelerating arc in a rather unique way. An understanding of these phenomena will lead to considerable insight into the parameters which make ablative plasma acceleration so unique.

3.5 Current Distribution

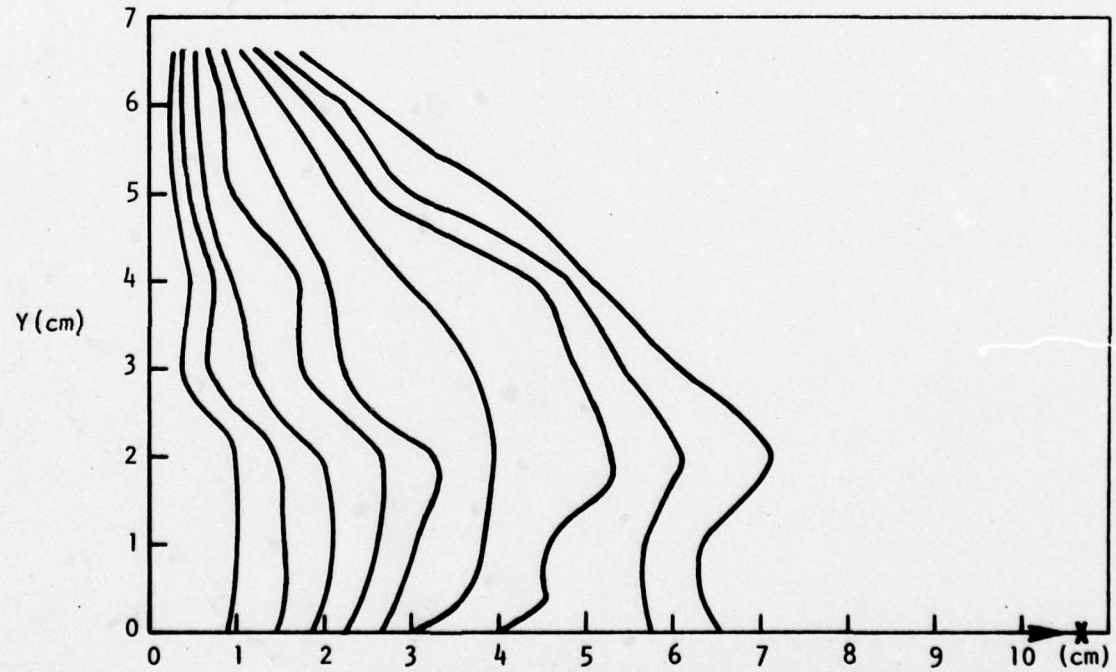
In order to obtain some idea of the current distribution within the plasma a Rogowski loop was constructed which could be positioned at known locations from the propellant surface along the centerline. Since the loop would be immersed in the hot plasma it was necessary to protect the winding by potting the entire coil with a high temperature epoxy after it was wound. The loop was rectangular in shape, having an inside width and length of 2 mm and 10.7 cm. The coil was designed so as to extend laterally slightly beyond the ends of the electrodes to insure that all current flowing through the plasma at a given location would be intercepted. The diameter of the winding, including the epoxy coating, was 2.8 mm. The coil was calibrated on the same circuit as that used to measure the total discharge current.

Data were obtained at each position scanned by discharging the capacitor bank and recording the total discharge current and the plasma current probe response simultaneously on the digital memory oscilloscope. The total discharge current was used to insure a consistent zero time reference for all data. It is noted that with the coil immediately up against the Teflon surface the center of the loop was 3.6 mm away from it. The current flowing at the ablation surface was obtained by extrapolating back using the two data points closest to it.

Figure 10 shows the distribution of current at four different times during the discharge. These four instants of time are the same as those at which magnetic flux was plotted. Figure 10a shows the distribution of current flowing through the plasma at 1.93 μs which corresponds to the instant at which peak discharge current occurs. The data is

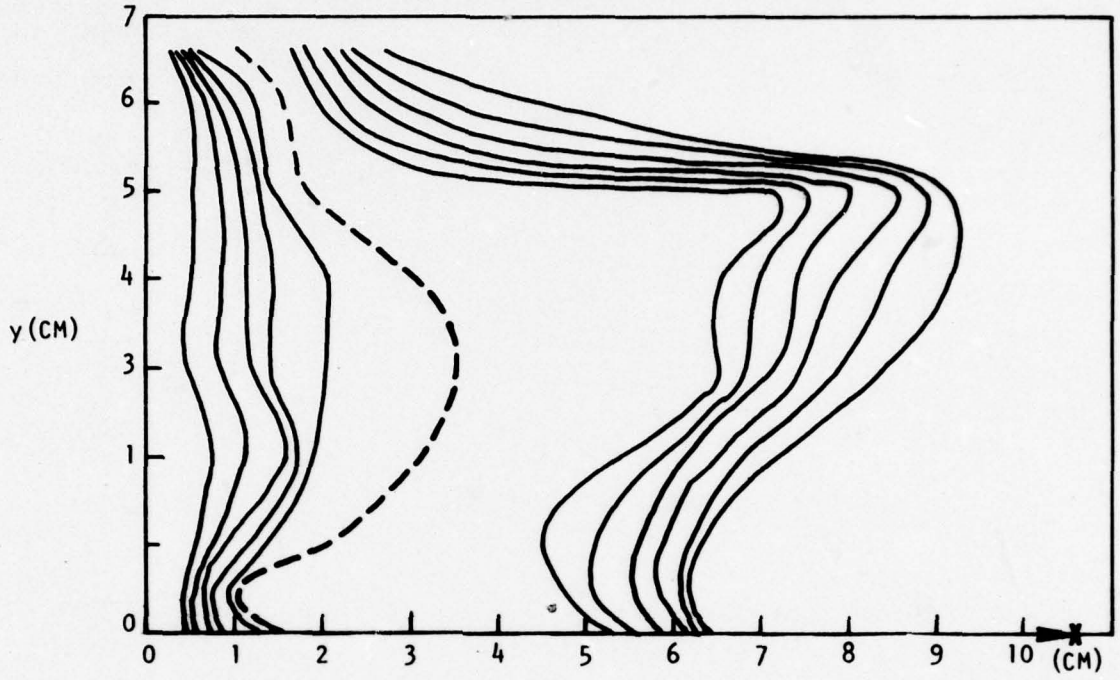


(a) t = 1.93 μs

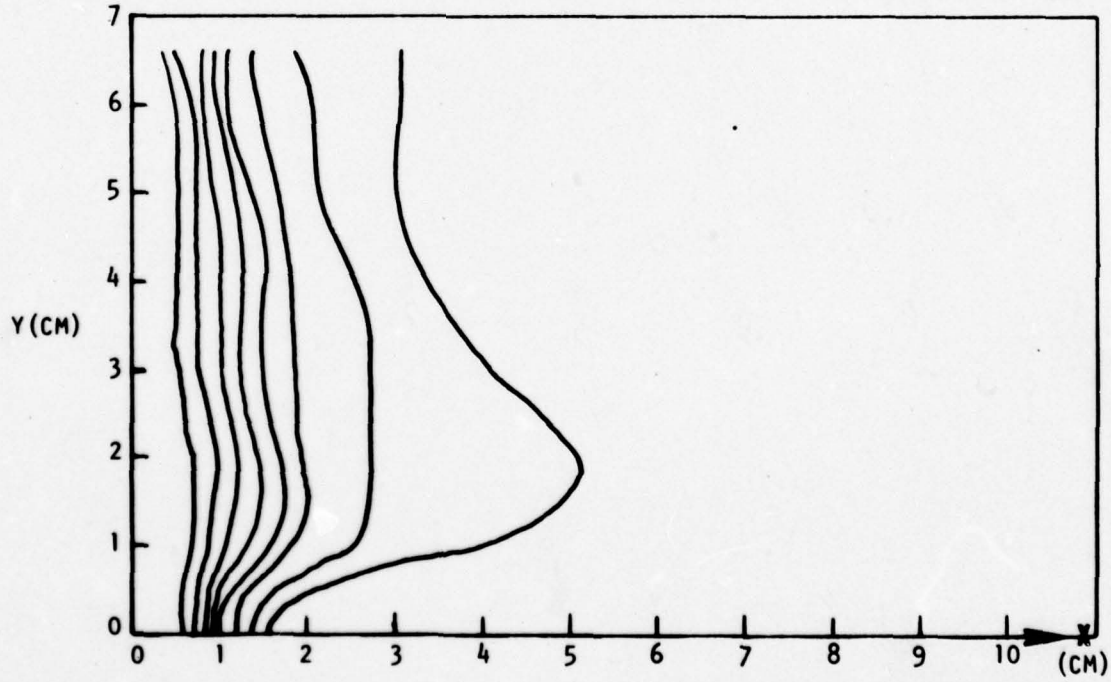


(b) t = 2.93 μs

Figure 10. Current Distribution at Various Times During Discharge



(c) t = 3.85 μs



(d) t = 4.85 μs

Figure 10. (Continued)

presented in the form of percentage contours, the line closest to x = o representing the farthest downstream position at which 20% of the total current flowing at that time is flowing through the plasma, and each subsequent line showing 10% increments of the total. The same presentation appears in Figure 10b at 2.93 μ s.

It is clear from Figure 10a that the discharge current is distributed fairly evenly throughout the arc in each plane parallel to the electrodes although significant variations in arc thickness are evident from one plane to the next. The arc is thicker at the cathode than at the anode, which is what estimates of the current density from the magnetic flux seemed to indicate. Having these two sets of data it is possible to calculate an average width of the arc at both the anode and the cathode. Calculation of J_2 using Equation (2) and the magnetic flux data yieleded values of 42 MA/m^2 and 25 MA/m^2 at the cathode and anode; respectively near the ablation surface. The current distribution indicates that near the cathode 20% of the 29.9 kA is flowing out to approximately 0.2 cm and near the anode this same amount of current is flowing out to 0.7 cm. These values lead to an estimate of 0.7 cm for the arc width at the cathode and 3.4 cm at the anode.

At 2.93 μs (Figure 10b) the current is still fairly uniformly distributed throughout the arc. Estimates of the arc width based on data at this time level are approximately the same as those values generated at 1.93 μs. The degree to which the arc leading edge at the anode is preceding the leading edge at the cathode is considerably more severe at this level of time, however. It is noted that the arc at the cathode has not advanced downstream at all during the one microsecond between Figures 10a and 10b, whereas there has been a movement of approximately 2.5 cm at the anode surface during the same time period. Comparison of the data in Figures 10a and 10b with the plasma front location determined using the time-of-arrival probe indicates that at 1.93 μ s the plasma front and arc leading edge are very close to each other at the anode and cathode surfaces but within the gap the plasma leading edge is ahead of the arc front as much as 1 cm at some locations. At 2.93 μs the situation is somewhat different, however. The plasma leading edge at the cathode surface is approximately 2.2 cm ahead of the arc front and at the anode the plasma leading edge precedes the arc front by some 1.3 cm. Within the gap one finds that the plasma leading edge is a maximum of 2.8 cm ahead of the arc front at y = 5 cm. These observations indicate that the plasma is indeed accelerating out ahead of the arc even as the arc itself spreads

downstream. This is attributed to the action of the Lorentz force on charged particles in the arc front. It is also noted that the locus of points at which the magnetic field is a minimum negative value corresponds quite well to the arc front location as would be suspected. Hence, those charged particles which are accelerated out ahead of the arc will find themselves in a favorable crossed electromagnetic field and will, therefore, continue to accelerate.

The data at 3.85 μs (discharge current reversal) is presented in a slightly different way because no current is flowing from the capacitors at that instant. Current is, however, flowing within the plasma but conservation of charge requires that no net current flow exist. This is indeed the case since the reversal of current flow direction within the plasma occurs roughly one half microsecond prior to total discharge current reversal and begins flowing in the opposite direction at the ablation surface. In Figure 10c, therefore, the dashed line shows the maximum downstream position up to which the current is reversed. The solid contours on either side indicate the extremities of various percentages of the total reverse current flow. Between x = o and the dashed line, the first solid contour shows 50% of the total and each subsequent line includes 10% more. To the right of the dashed line the first solid contour shows 50% and each subsequent line 10% less net current flow. The two separate distinct arcs which are formed as a result of the current reversing its direction of flow within the plasma prior to the reversal of total discharge current are clearly obvious in Figure 10c. Moreover, because of the close proximity of the two arcs near the cathod surface, it appears that there is indeed a closed current loop within the plasma at the time no net discharge current is flowing from the capacitor bank. The arc at the ablation surface is being sustained at this instant of time by energy previously deposited in the accelerating arc.

In Figure 10d, one microsecond after discharge current reversal, the data are again presented as percentage of total discharge current at that instant, the first contour representing 20% and each subsequent contour 10% more. This figure indicates that the accelerating arc has moved entirely out of the electrode gap and shows the existence of the developed second standing arc.

A point worth clarification with regard to the separating or degeneration of the initial arc into two separate arcs is the direction of accelerating forces just prior to this

occurrence. Let us trace the events from the time peak current occurs and consider only the Lorentz force on the plasma, which is proportional to the x-derivative of the square of the magnetic flux density (when $\partial B^2/\partial x$ is negative the Lorentz force is positive). Maximum flux density at the wall occurs at maximum discharge current, as observed from the data on B. Moreover, the values of B at the ablator are the local maximum values at any distance y above the anode. Hence, the gradient in magnetic pressure is negative up to the time peak current occurs and, therefore, the Lorentz force is directed away from the ablator, tending to accelerate the plasma. Consider now what happens as the discharge current decays from the maximum. The magnetic flux density at the ablation surface will also decrease from its maximum value. Due to the conductivity of the plasma, however, particles which have been ablated up until that time are carrying magnetic field energy with them away from the wall, and as these particles move further downstream the conversion of magnetic field energy into kinetic energy via the Lorentz force will cause the amount of magnetic field energy associated with each accelerating particle to decrease. The rate of decrease of magnetic field energy within a small region close to the ablation surface and the rate of decrease of magnetic flux density at the surface itself are the relevant parameters in determining what happens next. If these rates are comparable then the gradient in B^2 at the ablation surface will be small but favorable regarding acceleration, but as soon as the rate of decrease in B at the ablation surface is faster than the rate of energy conversion from magnetic to kinetic within the small volume close to the wall, the gradient of B will become adverse. Simultaneously the electric field at the ablation surface must change direction and the direction of current flow at this surface must reverse. The most interesting aspect of this is the fact that the total discharge current flowing from the capacitor has not changed its direction of flow at the time the gradient in B^2 has become adverse and hence, the vast majority of the plasma produced up until that time is still being accelerated with a favorable gradient in B^2 present within. The arc is, therefore, forced to split into two separate arcs, one carrying current in the same direction as the current flow from the capacitor, and one carrying current in the opposite direction. This leads to a closed current loop within the plasma which amplifies the magnetic field strength between them and produces as a result an "explosion" force distribution, tending to push the accelerating arc

out of the electrode gap and also tending to push the newly formed reverse current arc against the ablation surface. This can be more clearly visualized once it is realized that the direction of current flow at the ablation surface will reverse while the magnetic flux density is still positive and this implies a negative Lorentz force on the particles carrying the current. This situation persists only up until the time the total discharge current reverses, at which time the magnetic flux density also changes direction, and the forces on the standing arc become favorable regarding its acceleration. As nearly as can be estimated, the condition of negative Lorentz force on the second standing arc exists for approximately one half microsecond prior to discharge current reversal. That is, arc degeneration becomes incipient at about 3.3 μs subsequent to initiation.

3.6 Electron Number Density and Temperature

3.6.1 Description of Langmuir Probe

In order to measure electron number density and temperature within the accelerating plasma a conventional double Langmuir probe was constructed. The probe consisted of two strands of 5 mil (.126mm) tungsten wire enclosed within a glass rod. The length of wire exposed beyond the end of the glass rod was 1 cm (see Figure 11).

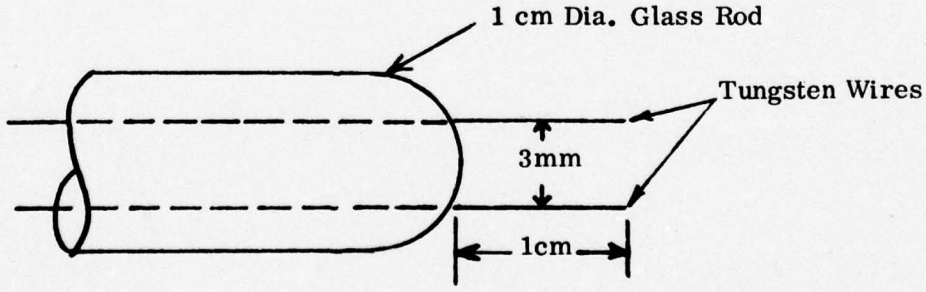


Figure 11. Langmuir Probe Configuration

Initial experimentation with this probe led to an unexpected problem associated with its utilization in the plasma produced from depolymerized Teflon. It was found that a tendency for the tungsten wires to become contaminated by the plasma was prevalent. Moreover, this contamination was severe enough to make acquisition of a single voltage/current characteristic impossible. A technique for remote cleaning of the probe wires would therefore have to be developed if experimentation was to continue.

The technique finally decided upon was to use electron bombardment of the probe wires. The electron source for this bombardment was a tungsten ribbon 5 mils (.127mm) thick and 20 mils (.508mm) wide wound in a helical fashion with three complete turns on a diameter of roughly 5 cm. The probe was positioned at the geometrical center of this winding and the ends of the ribbon were fastened to two standoffs fixed to the body of the probe. Experimentation with this arrangement resulted in the appropriate parameters necessary to do a good cleaning job on the probe wires. It was found that by running approximately 230W at 33 VAC through a transformer directly to the tungsten ribbon and at the same time maintaining a DC voltage of 1900 to 2300V on the probe wires, a current of about 70MA would pass from the ribbon to the probe, which was sufficient to heat the probe wires to red hot in 10 seconds. The final steady state temperature of the tungsten ribbon was 2400°C, measured using an optical pyrometer. The probe voltage, once fully heated, dropped to 1000 VDC. The circuit used to clean the probe wires is depicted in Figure 12.

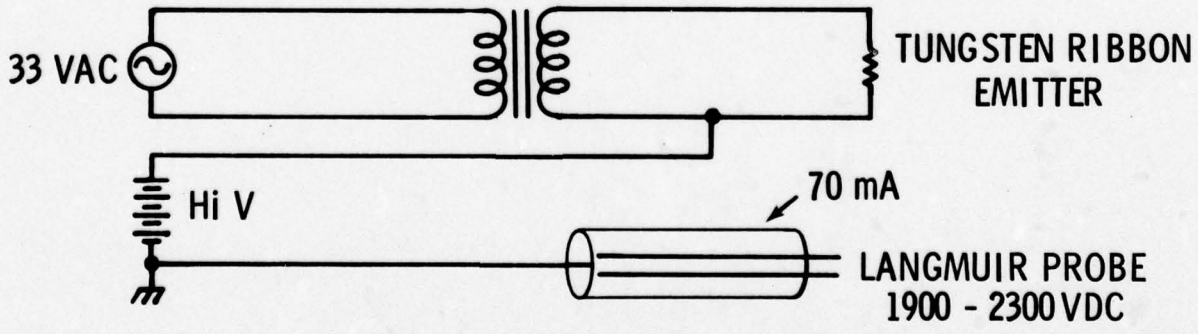


Figure 12. Schematic of Probe Cleaning Circuitry

A secondary result of cleaning the probe wires was local destruction of the glass rod enclosure near the point from which the wires protruded. In order to preserve the lifetime of a given probe this localized erosion had to be minimized so a second glass enclosure in the form of a 2cm ID tube was placed around the glass rod such that the end of the tube was just ahead of the end of the glass rod. This solved the problem of local destruction at the end of the glass rod. A photograph of the final Langmuir probe configuration with remote cleaning capability built in is presented in Figure 13.

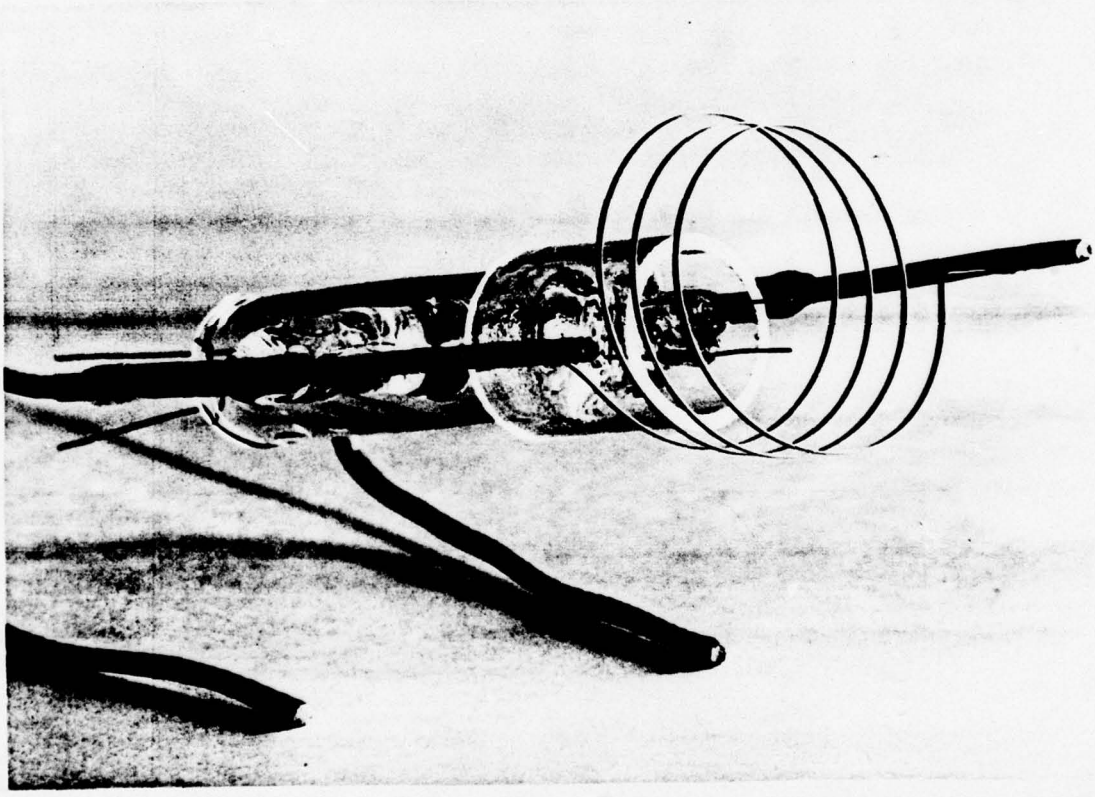


Figure 13. Langmuir Probe Equipped for Remote Cleaning by Electron Bombardment

3.6.2 Data Acquisition Procedure

In order to measure electron number density and temperature at a given point within a plasma it is necessary to obtain a complete voltage/current characteristic at that point. A good characteristic has the shape of an arc tangent function, asymptoting the ion saturation values of current as the applied voltage is made

large positive or negative, and crossing through the origin of the IV-plane. Under conditions of a plasma which is either quiescent or moving at a constant speed one can normally pulse the probe with a voltage ramp function of short duration and display I vs. V at the probe on an oscilloscope having appropriate frequency response. In a transient situation, however, use of the pulsed probe technique would require considerable developmental effort to manufacture a driver to generate a voltage ramp of sufficient magnitude in the short time period necessary to obtain a reasonable degree of resolution (i.e.; typically -20V to +20V in approximately 1 microsecond). The development of such a driver was beyond the scope of the current program so an alternate method of data acquisition was formulated.

The technique used on this program consisted of locating the probe at the desired position, applying a DC voltage of known magnitude across it, and firing the accelerator. Current drawn from the DC source as the plasma passed the probe was detected using a precalibrated Rogowski coil. Discharge current and the probe current were simultaneously displayed on a Tektronix dual beam oscilloscope. The discharge current provided a common time base to which all data could be referenced. A new oscillograph is recorded for each DC voltage applied across the probe and reduction of the data to a voltage/current characteristic at a given time subsequent to arc initiation is accomplished by converting the probe signal trace to current at that instant of time for each of the applied voltages. Typically, up to ten different DC voltages are applied at any given location in order to generate the characteristic. A typical volt-ampere characteristic obtained as outlined above is presented in Figure 14.

3.6.3 Data Reduction

The electron number density and temperature are related to the volt-ampere characteristic by simple probe theory through the following two relationships:

$$\left(\frac{dI}{dV}\right)_{v=o} = \frac{I_{sat}}{2T_e}$$

$$I_{sat} = \frac{1}{2}\, n_e\, Ae\, (11{,}606kT_e/M_+)^{\frac{1}{2}}$$

where I is current, V is voltage, I_{sat} is the ion saturation current (assumed symmetrical), T_e is the electron temperature in ev, n_e is the electron member density, A is the probe collector area, e is the electron change, k is the Boltzman

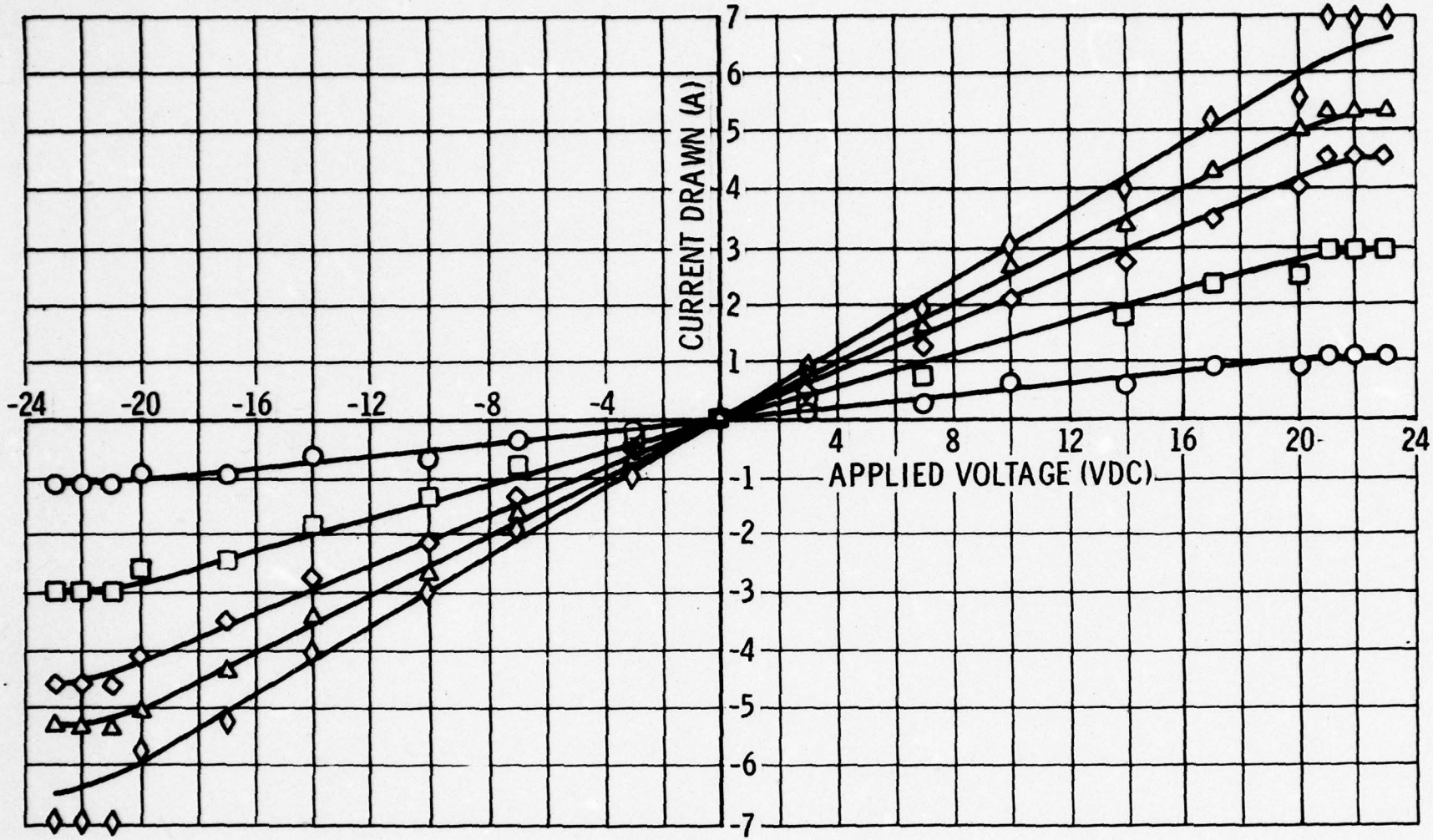


Figure 14. Typical Volt-Ampere Langmuir Probe Characteristic

FAIRCHILD
REPUBLIC COMPANY

constant and M_+ is the ion mass. In this particular case the collector area is .0157 cm^2 and the ion mass is estimated as being the equivalent of a 2C + 4F gas mixture or 16.67amu. Thus;

$$n_e = 1.652 \times 10^{15} I_{sat}/T_e^{\frac{1}{2}}$$

with n_e expressed per cubic centimeter, T_e in ev and I_{sat} in amperes.

3.6.4 Number Density and Temperature Distribution

The modifications made to the probe as outlined in section 3.6.1 in order to keep the probe collectors clean made it impossible to scan across the interelectrode gap between the anode and cathode because of space limitations. It was, however, possible to scan along the centerline in the axial direction but the degree to which this could be accomplished was curtailed by the fact that we could not get closer to the ablator surface than 5 cm. The reason for this was the severe electrical noise generated in the probe circuitry by the arc initiation. The results of measurements made along the accelerator centerline are presented in Figure 15 where electron number density as a function of distance is plotted at various times. These curves indicate a continuous monotonic decrease in electron number density with downstream distance. The overall level of the number density is increasing with time as the arc progresses downstream. The maximum value of the number density which was measured is $1.46 \times 10^{15}/cm^3$. If one were to linearly extrapolate this value back to the surface of the ablator, a number density of $2.62 \times 10^{15}/cm^3$ would be obtained.

The presence of conducting plasma as a function of time at a given point can be more or less interpreted from the Langmuir probe response at that point. A typical oscillograph of this response, as well as the discharge current has been reproduced in Figure 16. Note the appearance of a very clearly defined region of conduction between 6 and 10 microseconds after discharge initiation. The probe response during this interval is more than likely due to the passage of the first plasmoid. One can also interpret the peak at 14 microseconds as being due to the arrival of the second plasmoid.

The electron temperature along the centerline of the accelerator was found to be constant within the accuracy of the experimental results. A value of 10ev is characteristic and did not vary in space or time. This result is not surprising but is meaningful because it indicates that the energy equipartition time for electron/ion

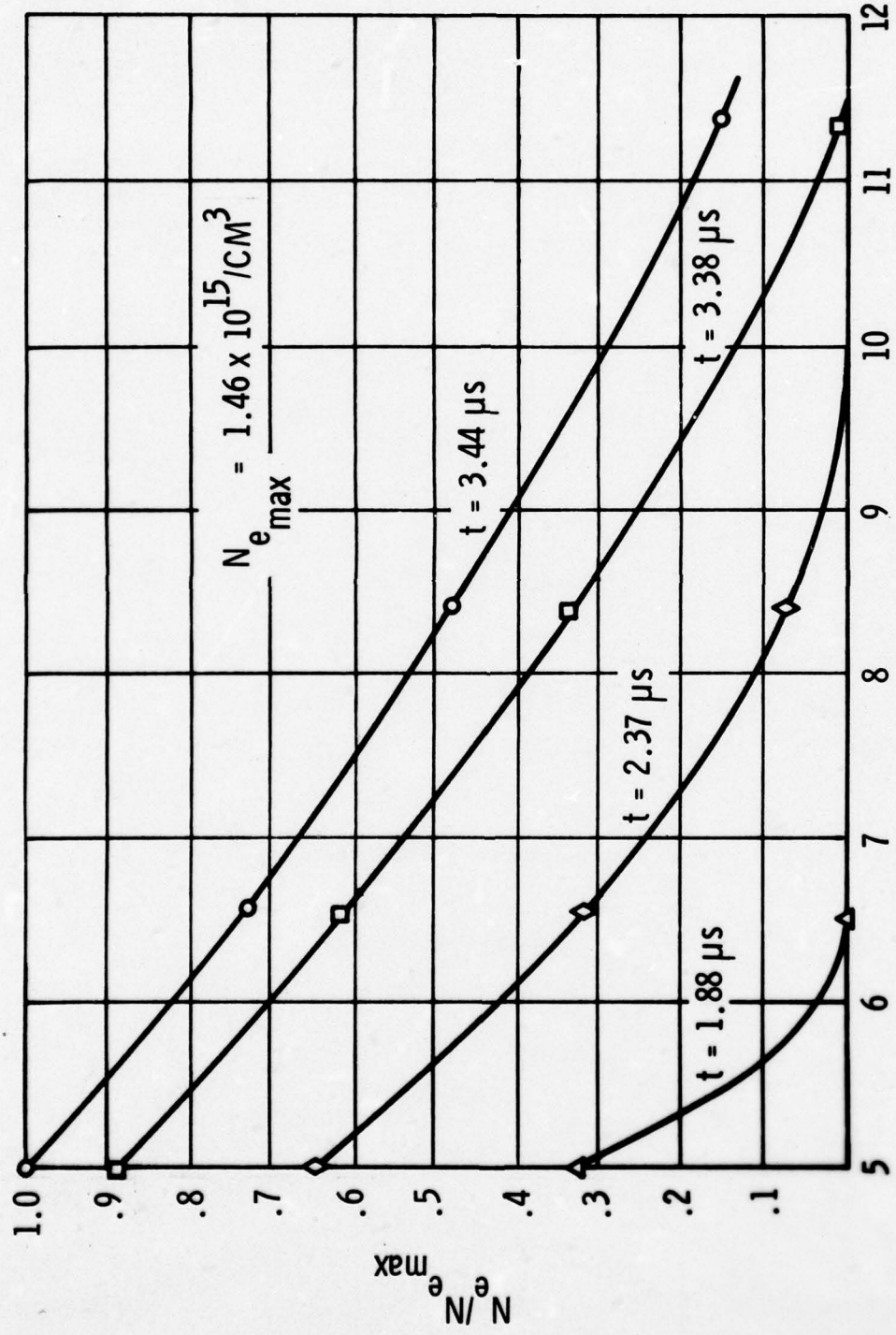


Figure 15. Electron Number Density as a Function of Distance Along the Accelerator Centerline at Three Different Times

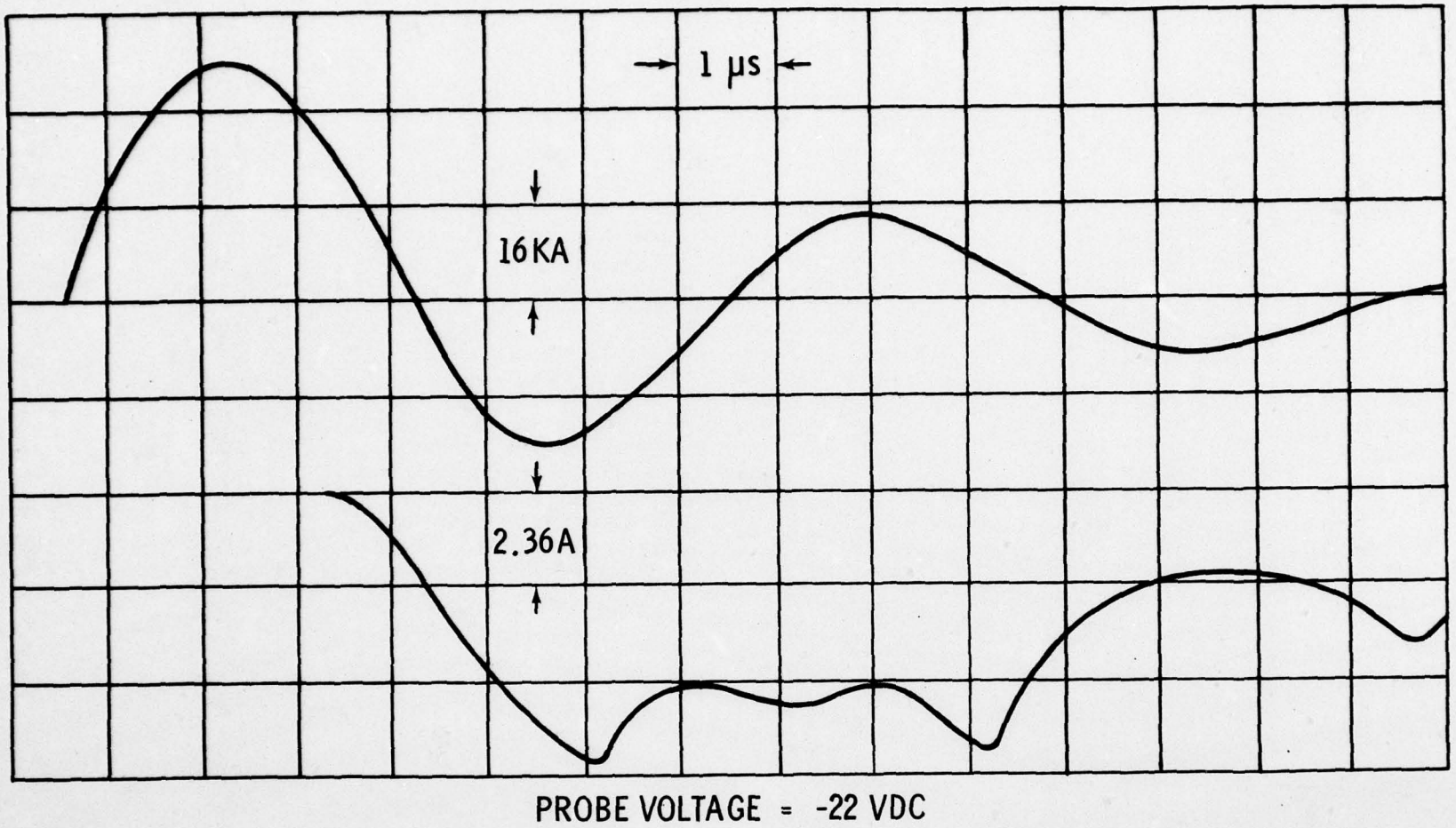


Figure 16. Typical Langmuir Probe Response and Discharge Current 2cm Past the Electrode Exit Plane

FAIRCHILD

thermalization is much longer than the characteristic flow time in this accelerator.

A two dimensional scan across the interelectrode gap was also performed at a distance of 2cm beyond the exit plane of the electrode. Space limitations within the test facility limited the region scanned to approximately 2cm on either side of the centerline. The contours as a function of lateral position at three different times are presented in Figure 17. These contours all show a local maximum in electron number density near the centerline of the accelerator and a rapidly decreasing level as the cathode is approached. As the anode is approached the electron number density first decreases and is then seen to be increasing. This result is as one would normally suspect in an arc of this type except for the local minimum at 5cm which is probably more related to the flow dynamics than to the distribution of fields.

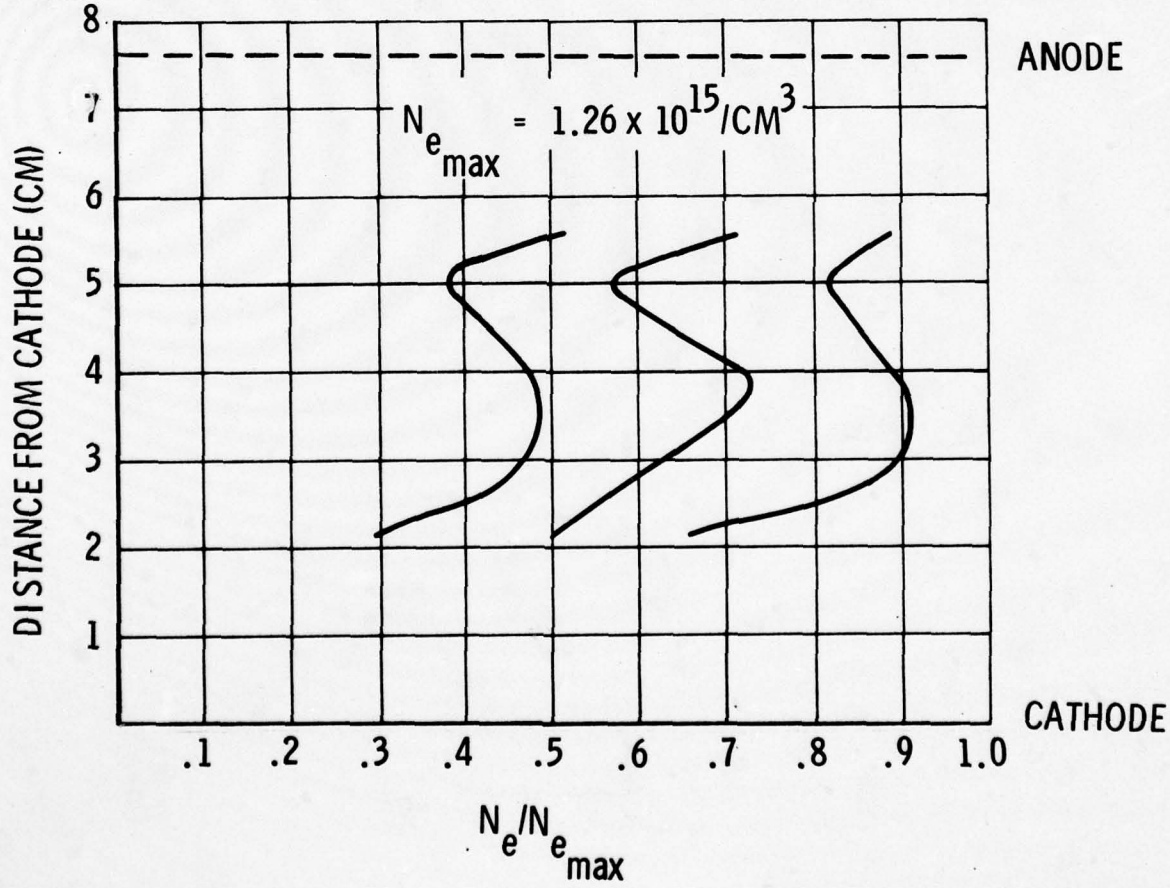


Figure 17. Electron Number Density Across the Interelectrode Gap a Distance 2cm Past the Electrode Exit Plane

4.0 THEORETICAL APPROACH

4.1 Physical Model

The basis for the physical model used to obtain an analytic representation of the plasma acceleration mechanism in pulsed ablative thrusters is the assumption that the plasma can be considered a continuum at all points in space and for all time. Such a model results in a complete description of the plasma by specification of its macroscopic thermodynamic properties. Changes in the values of these properties are governed by a set of conservation equations which are derived for mass, momentum, and energy. These equations are valid in their complete form for the solution of any flow problem and only the boundary and initial conditions determine precisely which problem is being solved. The consistency and accuracy of the initial and especially the boundary conditions is therefore essential to obtaining an analytic solution to the governing equations which accurately describes the physical process being modeled.

The thermodynamic state of the plasma is assumed to be a combination of ions, neutrals, and electrons, each of which is in local thermodynamic equilibrium but thermodynamic equilibrium between ions and electrons is not assumed to exist while ions and neutrals are assumed to be in equilibrium with one another. The three species are considered to be moving at the same baricentric velocity and local charge neutrality is assumed.

4.1.1 Initial Conditions

A detailed model of the breakdown or "initiation" phase of the discharge would be required if one desired to begin calculation of the plasma flow precisely at time $t = 0$. Since no such model exists at this time for the breakdown mechanism used in pulsed ablative thrusters (i.e., the ignitor plug discharge of a microplasma into the interelectrode gap) it is not possible to begin calculation at precisely $t = 0$. Instead, calculations begin at time subsequent to $t = 0$ when it is believed that the solid Teflon propellant first begins to depolymerize into gaseous molecules. This occurs approximately 100 nanoseconds after initiation, at which time roughly 600A are flowing through the fully developed arc. Up until this time the arc is probably supported mostly by the microplasma injected by the ignitor plug and to some degree by consumed electrode material. The arc thickness at the time calculations are commenced is obtained by linear extrapolation of the early experimental data to that

time. The resulting arc thickness obtained in that fashion is 2mm and the arc width is 3cm. The current density of 10 MA/m^2 is assumed to be uniformly distributed from the ablation surface to the downstream extremity of the arc. The magnetic flux density has parabolic decay from its value at x = o to its value at the leading edge. These values are computed as described in the next section. The initial energy per unit volume is taken as the energy deposited into the arc up until 100ns divided by the volume ($4.57cm^3$). The initial arc is assumed to have zero velocity and uniform thermodynamic pressure and mass density, obtained by subtracting the magnetic field energy from the initial energy input and assuming a temperature of 10ev.

4.1.2 Boundary Conditions

The coordinate system is located with its origin at the center of the interelectrode gap on the ablator surface at the midpoint of the ablator. The x-coordinate is positive along the centerline of the electrodes with positive y directed along the ablator surface (toward the cathode) and positive z parallel to the electrodes. The assumption of two dimensional motion negates variations of all dependent variables in the z direction.

The mathematical problem is to find the solution to Equation (3) with initial conditions specified in the domain $o \leq x \leq \infty$ for all $-\frac{1}{2}h \leq y \leq +\frac{1}{2}h$. The existence of diffusion terms in Equation (3) makes them a parabolic set, having only one characteristic direction, namely streamlines, given by $dx/dt = u$ and $dy/dt = v$. Since the direction of propogation of this characteristic will always be away from the ablator surface (i.e., $u \geq o$ always) it is necessary to specify a number of relationships among the dependent variables equal to the number of dependent variables at $x = o$ for all y between $-h/2$ and $+h/2$. Moreover, since streamlines will always propogate away from the electrode surfaces due to the probable existence of boundary layers, all dependent variables having second derivitives in the y-direction must be specified on $y = \pm h/2$ for all $x \leq \ell$. These include B, u, v and T. Similarly, these dependent variables must also be specified ahead of the plasma for all time.

The velocity of ablated Teflon at the instant depolymerization occurs must be zero since prior to that time the gaseous particles will not have experienced any imbalance of forces which could cause them to accelerate. Hence, the conditions $u = v = o$ must exist at the ablation interface for all time.

The temperature at the ablation surface has been measured under controlled thermal degradation experiments. It was found that the temperature of the solid just prior to its sublimation is not a function of the heat flux impingement upon it and is equal to 640°C. Thus, a constant temperature surface is assumed at the ablator.

In order to generate a boundary condition on the density it is necessary to resort to a previously published empirical data correlation between the total mass ablated

per discharge and the integral of the square of the discharge current over time [16]. It was shown that to a fair degree of accuracy a significant amount of data obey the relationship

$$m = \alpha \int_0^\infty i^2 dt$$

The constant α was determined precisely for the experimental apparatus used throughout this program. With the integral of current squared being $1.92 \times 10^3 A^2 s$ and a mass per discharge (averaged over 1000 discharges to within $\pm .2\mu$ g) of 0.148 mg, the constant α is 7.7×10^{-8} g/A^2s. Extending this correlation to imply that at any instant of time t

$$m(t) = \alpha \int_0^t i^2 dt$$

leads to the conclusion

$$\dot{m} = \alpha i^2$$

Furthermore, by assuming a uniform ablation of the propellant surface, the instantaneous mass flow rate per unit area can be obtained by dividing $\dot{m}$ by the propellant area A_p. The density at each grid point on the ablation surface is calculated using a variation of the finite difference scheme outlined in the Appendix. Letting the set (i, j) represent a point on the ablator, a control volume of length Δx and height $2\Delta y$ is chosen such that the four corners of this volume are (i, j + 1), (i, j -1), (i + 1, j + 1), and (i +1, j -1). The density at the point (i + $\frac{1}{2}$, j) is then calculated to second order accuracy in time and space by invoking the conservation of mass in this fixed volume. The resulting expressions are

$$\rho_{i+\frac{1}{2},j}^{K+1} = \rho_{i+\frac{1}{2},j}^{K} - \frac{\Delta t}{2\Delta x}\left[(\rho u)_{i+1,j}^{K+1} + (\rho u)_{i+1,j}^{K}\right] - \frac{\Delta t}{4\Delta y}\left[(\rho v)_{i+1,j+1}^{K} - (\rho v)_{i+1,j-1}^{K} + (\rho v)_{i+1,j+1}^{K+1} - (\rho v)_{i+1,j-1}^{K+1}\right]$$

and

$$\rho_{1,\frac{1}{2}}^{K+1} = 2\rho_{1+\frac{1}{2},\frac{1}{2}}^{K+1} - \rho_{1+1,\frac{1}{2}}^{K+1}$$

The above can be used at all points on the ablation surface except those points in the corners. To obtain the density at the two corner points values at the two adjacent points on the ablation surace are extrapolated.

The thermodynamic pressure at the ablation surface is obtained from the equation of state. A gas constant consistent with fully dissociated gaseous Teflon (i.e., 2C + 4F) having a mocular weight of 16.67g/mole is used throughout.

The boundary condition on magnetic flux density at the ablation surface is related to the condition at the leading edge of the accelerating plasma at each time step for each value of y through Amperes circuital law

$$\oint \bar{B} \cdot d\bar{l} = \mu I$$

where integration is carried out over any closed path and I is the current flowing through the enclosed surface. Assuming the width of the plasma in the z-direction is w, and denoting the position of the leading edge of the plasma at each value of y by $x_o(y)$ the integration around a rectangular path in the xz-plane gives

$$w\left[B_3(0,y,t) - B_3(x_0,y,t)\right] + \int\left[B_1(x,\tfrac{w}{2},t) - B_1(x,-\tfrac{w}{2},t)\right]dx = \mu I \qquad (2)$$

which must be satisfied at each value of y. B_1 and B_3 are the x and z components of magnetic flux; respectively. No variation of B_3 in the Z-direction is implied in the above equation, but, nevertheless, the problem does assume a certain degree of three dimensionality since magnetostatic field components will and do exist in the space around the plasma because the acceleration discharge path is such that external fields are not cancelled. The external fields are due to the flow of current through the plasma itself and can be determined once the current density throughout the plasma is known. The relationship which must be evaluated is

$$\bar{B}(x,y,z) = \frac{\mu}{4\pi}\int_{-\frac{w}{2}}^{\frac{w}{2}}\int_{-\frac{h}{2}}^{\frac{h}{2}}\int_{0}^{x_0}\frac{\bar{J}\times\bar{r}}{|\bar{r}|^3}dx'dy'dz' \tag{3}$$

The values of B_3 used in Equation (2) will be assumed to be those values at the center of the arc ($z = o$). Thus, for $x = x_o$.

$$B_3(x_o,y,o) = \frac{\mu w}{4\pi}\int_{-\frac{h}{2}}^{\frac{h}{2}}\int_{0}^{x_0}\frac{[J_1(y-y') - J_2(x-x')]\,dx'dy'}{r^2\sqrt{r^2+\frac{w^2}{4}}} \tag{4}$$

where $$r^2 = (x_o-x')^2 + (y-y')^2$$

The values of B_1 in Equation (2) are evaluated at the outer extremities of the arc. These are given by

$$B_1(x,y,\tfrac{w}{2}) = \frac{\mu}{4\pi}\int_{0}^{x_0}\int_{-\frac{h}{2}}^{\frac{h}{2}} J_2\left(\frac{1}{R}-\frac{1}{r}\right)dx'dy'$$

$$B_1(x,y,-\tfrac{w}{2}) = \frac{\mu}{4\pi}\int_{0}^{x_0}\int_{-\frac{h}{2}}^{\frac{h}{2}} J_2\left(\frac{1}{r}-\frac{1}{R}\right)dx'dy'$$

Since $$B_1(x,y,-\tfrac{w}{2}) = -B_1(x,y,\tfrac{w}{2})$$

it is only necessary to evaluate one of the above and integrate it from $x = o$ to $x = x_o$, using twice the value of the resulting integral in Equation (2).

Having set up the integrals in analytic form it is now necessary to generate a technique for evaluating them numerically at each time step. The trapazoidal rule for numerical

integration is used. This leads to rather lengthy formulas and for brevity only the functional form of a typical integral is presented below.

$$\iint F(x,y)\,dx\,dy = \sum_{\lambda=1}^{N}\sum_{j=1}^{M}\left(F_{\lambda+1,j}+F_{\lambda-1,j}+F_{\lambda,j+1}+F_{\lambda,j-1}\right)\frac{\Delta x\,\Delta y}{4}$$

The above procedure leads to values of B_3 at $x = x_o(y)$ and $B_1(x, y)$ between $x = o$ and $x = x_o$ which are themselves functions of $B_3(o, y)$ for each value of y. This results because unless $B_3(o, y)$ is known for each value of y it is not possible to calculate the current density at the point $x = \Delta x$ using a central difference approximation. Thus, if M is the number of grid lines in the y-direction, one arrives at M simultaneous linear algebraic equations for the M values of B_3 (o, y); $y = -\frac{1}{2}\,M\Delta y$ to $y = +\frac{1}{2}\,M\Delta y$. This occurs at each level of time $k\Delta t$. The numerical solution uses Gausian elimination to solve this set of equations for the values of B at the ablating wall. Knowing the conditions on ρ, u, v, p and B at the ablator surface allows calculation of the dependent variables vector W.

The leading edge of the accelerating plasma is defined as that point at which the density is smaller than some arbitrarily small value which is held constant throughout calculations. Ahead of this point all values of ρ are set equal to zero to simulate the true vacuum condition. Similarly, all other dependent variables are zero ahead of the plasma except of course the magnetic flux density which must decrease in magnitude from its value at the leading edge to zero as x approaches infinity. The value of B at the leading edge is obtained at the same time the values at the ablation surface are obtained, but since the numerical calculation of the plasma motion in the neighborhood of the leading edge requires three additional values of B, i.e., namely those at $x_o + \Delta x$ and $x_o + 2\Delta x$, Equation (4) is utilized twice more to obtain these required values. It is noted that in truth the equation governing the magnetic flux density ahead of the plasma is wave-like with the propogation speed equal to the speed of light. Utilizing a magnetostatic field equation ahead of the plasma front is, therefore, only an approximation to the real state of affairs but is an excellent

approximation when the front velocity is not relativistic, as is the case in this device. Essentially this approximation requires that the unsteady redistribution of flux density ahead of the plasma occurs at essentially infinite speed when compared to the speed at which the plasma leading edge is moving or the speed at which the value of B at the leading edge is changing. This is in fact the present case since the speed of light is roughly four orders of magnitude larger than the plasma velocity.

Conditions on the electrode surfaces are considered next. The fact that the electrodes represent impervious surfaces requires that the normal component of flow velocity be zero. Regarding the tangential component, however, a careful evaluation of the continuum boundary condition is warranted. Normally, when a fluid is assumed to have finite viscosity the tangential component of velocity is set equal to zero on a boundary surface. It is known, however, that under certain conditions this boundary condition is not valid and a certain amount of fluid motion tangential to the surface does exist. When these conditions exist a so-called "slip" boundary condition is applied as opposed to the usual "no-slip" continuum situation. The parameter which is relevant in determining whether slip or no-slip is applied is the local mean free path. The larger the mean free path, the less valid a no-slip assumption becomes. Velocity at the surface of the wall is given by

$$u_w \propto \lambda \left| \frac{\partial u}{\partial y} \right|$$

where λ is the mean free path. Under conditions of low wall density, the velocity at the wall's surface will not generally be small as compared to velocities elsewhere.

The electrode surface temperature will be considered a constant during the discharge period. The value of the temperature is set just below the electrode melting point. For copper this is 1335°K. The electrode boiling point is used only in the region which the plasma exists. Ahead of this the electrode temperature is assumed to be room temperature (297°K). The boundary condition on magnetic flux density is obtained from conditions which must be satisfied by the electric field. Namely, if the plasma is assumed to have a relative permitivity of unity, the tangential component of electric field at the electrode/plasma interface must equal zero. This condition, along with the fact that v = o at the electrode surface, leads to the result that there can be no component of current density tangential to the electrode surface.

Hence, the normal derivitive of the magnetic flux density must be zero at the electrode surfaces. Utilizing this condition together with internal known values of B yields the value of B at each point on the electrode surfaces. A scheme similar to that used at the ablation surface is used to calculate the density at the electrode surfaces.

4.1.3 Plasma Coupling to Discharge Circuitry

The discharge circuit, consisting of the energy storage capacitor bank and strip line assembly connecting the bank to the electrodes, has certain capacitance, resistance, and inductance associated with it. The plasma represents the load through which this circuit is completed in series. Finite plasma conductivity and self induced magnetic field yield values of effective plasma resistance and inductance which must be included in the circuit equations so as to simulate the physical coupling of the plasma load and capacitor bank. Both the plasma resistance and inductance are functions of time, however, since the plasma motion is unsteady. Moreover, a nonlinear coupling which is not explicitly obvious in either the circuit equations or the conservation equations arises because the boundary conditions on mass flow rate of ablated teflon and magnetic flux density are functions of the discharge current at any instant of time, which, in turn, is a function of the temporal variations of plasma resistance and inductance up until that time. Thus, it is necessary to solve the circuit equations and conservation equations simultaneously to include this physical coupling via boundary conditions. In order to set up the appropriate circuit equations the schematic diagram shown in Figure 11 is postulated as being the appropriate equivalent circuit.

Expressions for the plasma resistance and inducatance are derived from the basic definitions of these quantities. One obtains the following expressions from these definitions:

$$L_p(t) = \frac{1}{i}\int_{-\frac{h}{2}}^{\frac{h}{2}}\int_{0}^{x_b} B(x,y,t)\,dx\,dy \qquad (5)$$

$$R_p(t) = \frac{1}{w}\int_{-\frac{h}{2}}^{\frac{h}{2}}\left[\int_{0}^{x_b}\sigma(x,y)\,dx\right]^{-1} dy$$

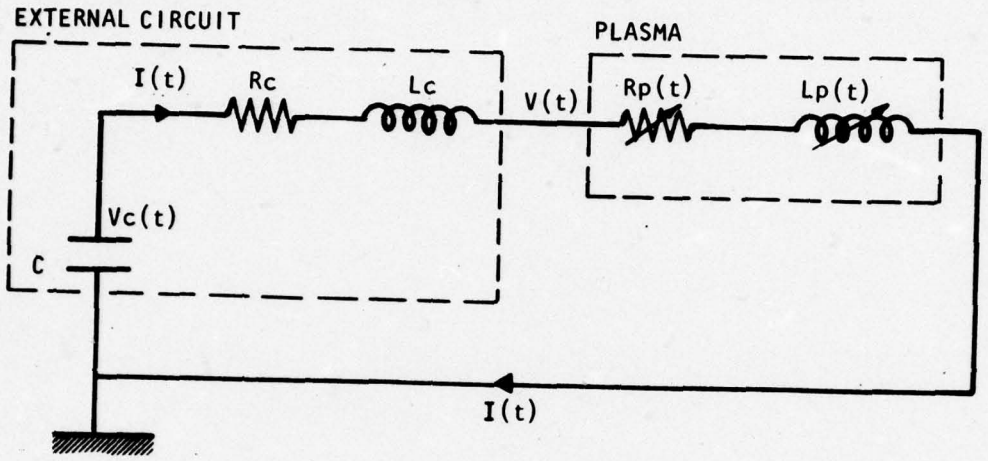


Figure 18. Equivalent Circuit Schematic

The circuit depicted in Figure 18 has the following set of simultaneous first order differential equations associated with it:

$$V(t) = [R_c + R_p(t)]\, i + \frac{d(L_p i)}{dt} + L_c \frac{di}{dt}$$

$$i(t) = -C \frac{dV}{dt} \qquad (6)$$

where V(t) is the potential difference across the capacitor terminals. Equations (6) are solved using the second order accurate Runge-Kutta technique with the integrals in Equations (5) evaluated to order $(\Delta x)^2$, $(\Delta y)^2$ using the trapezoidal approximation. The initial conditions on Equations (6) are i = o and $(di/dt) = V_o/L_o$ at t = o where L_o is the sum of L_c and $L_p(o)$ determined from the initial arc conditions derived in the previous section.

4.2 Governing Equations

The unsteady fluid dynamic conservation equations with two dimensions of spatial freedom may be written quite generally in the following form:

$$W_t + f_x + g_y = F_x + G_y + S \tag{7}$$

where W is a column vector containing the dependant variables; f and g are the advection vectors and are functions of W only; F and G are the dissipation vectors which are functions of W and its first spatial derivitives; and S is the source vector, a function of W only. The number of dependant variables (elements in W) is related to the particular fluid model being considered. In its simplest form, that is for a fully ionized one species plasma, W will contain only five elements, these being the density, momentum flux in both directions, total energy per unit volume, and magnetic flux. Generalizing the model to a two-fluid plasma in which ions and electrons are not in thermodynamic equilibrium but are moving at the same speed adds an additional dependant variable; namely, the electron energy per unit volume. If one further generalizes the model to include a third fluid (neutral gas species) which is in thermodynamic equilibrium with the ion species then the ionization kinetics determine whether or not an additional dependant variable must be solved for. Equilibrium ionization does not necessitate addition of another solution variable since the chemical composition of the plasma can be solved for using the algebraic equations of equilibrium kinetics. Essentially, such a kinetic model assumes that all ionization reactions are occurring infinitely fast in both the forward and reverse directions so that the chemical aggregation of the plasma can adjust to changes in the thermodynamic properties at each point in space-time as quickly as the flow requires. The assumption of finite rate ionization does require that an additional variable be included. Namely, the ion or electron density when local charge neutrality is assumed. Moreover, if more than one molecular neutral gas species is present, and finite rate dissociation and recombination is presumed to exist, one must also include the neutral gas density of each species in the vector W.

The model used herein does include a neutral gas species and presumes finite rate ionization but does not include the existence of more than one molecular species. The gaseous products produced by depolymerization of solid tetrafluorethylene (TFE) are indeed composed of many different probable species as will be shown in the next section of this report, but these various neutral molecules have been more or less

lumped together for reasons which are explained therein.

The resulting set of eight conservation equations (based upon the above discussion) are defined by the vectors presented in Appendix A of this report, wherein the effects of finite electrical and thermal conductivity as well as finite viscosity are manifested in F and G whereas finite rate ionization and therodynamic nonequilibrium are indicated by the nonzero elements of the source vector.

4.3 Chemical Model

As part of this research effort a detailed study was performed in which the probable chemical kinetics associated with gaseous decomposed TFE was analyzed. The results of that study are presented in this section.

With regard to the chemical composition of the plasma produced by sublimation of solid TFE very little information is available in the literature. Most of the information which is available has been generated via vacuum, air, or inert gas pyrolisis at relatively low radiative heat flux.[11-16] Perhaps the most relevant piece of work reported in the literature was performed by Mathias and Miller[17] wherein the decomposition of TFE in a glow discharge was studied using helium, helium plus oxygen, and pure oxygen as a carrier gas. It was determined that in the absence of oxygen the major constitutents in the depolymerized gaseous products are C_2F_4 (85.22%), C_2F_6 (6.43%), n-C_3F_6 (5.90%), C_3F_8 (2.08%), and CF_4 (0.37%). It was also determined that the basic sublimation process includes unzipping via CF_2 radicals, polymer formation via C_2F_4 excited species, and CF_2 radical disproportionation to account for the F species. The reactions thought to be most responsible for sustaining the discharge are

$$e + CF_2 \quad CF^+ + F + 2e$$

$$e + C_2F_2 \quad C_2F_4^+ + 2e$$

Because of the low ionization potential (10.3 ev), C_2F_4 is undoubtedly a major contributor of additional electrons during the "avalanche" phase of arc development subsequent to breakdown.

The thermophysical properties relevant to ablation of TFE have been the subject of more thorough investigation than has the chemical kinetics of the ablation products (see, e.g., Refs. 16, 18). These studies are of interest since they have provided some relevant information. All investigators cited are in agreement that the

ablation kinetics are first order, conforming to an Arrhenius formula for the ablation rate as a function of temperature. A general picture of the sublimation process consists of solid TFE passing through a "gel" state at 327°C in which the polymer bonds are unzipped (depolymerization) and the monomer is converted to CF_2 radicals. This gel remains in contact with the solid surface and becomes gaseous at a temperature of 640°C independent of the rate of heating.[18] The heat of ablation quoted in the literature varies from 333.4 and 424.0 cal/g. A mean value of 376.8 cal/g has been used herein. Interestingly, the total energy required to ablate the .148 mg of Teflon generated during a single discharge turns out to be only about one quarter of a joule based on this heat of ablation. With a discharge energy of 82J this is an insignificant fraction of the energy deposited in the plasma.

The chemical kinetic model postulated herein presupposes that the products of ablation are initially composed of 100% monomer. Justification for this assumption is derived from the fact that even during the extremely low energy glow discharge of Mathias and Miller only about fifteen percent of the products were observed to be other polymers. At substantially higher heat flux Settlage and Siegle observed even less (3-5%) amounts of other polymers. It is therefore more than likely tht all polymers are decomposed at the level of heat flux experienced by the ablation surface in this device. The gas composition at the ablation surface is therefore presumed to be 100% monomer at 640°C and is invariant with time.

Formulation of the chemical model proceeds by writing down all possible dissociation reaction leading to molecules having smaller molecular weight than C_2F_4. Calculation of the dissociation energy for each reaction is then performed by taking the difference in heats of formation between products and reactants. Heats of formation for the molecules considered were taken from the JANAF Thermochemical Tables. These are referenced to zero degrees Kelvin. The result of the above procedure is presented below where possible reactions and associated energy expressed in kcal/mole are listed.

(a) $C_2F_4 \rightleftharpoons C_2 + 2F_2 - 350.5$

(b) $C_2F_4 \rightleftharpoons 2CF_2 - 94.0$

(c) $C_2F_4 \rightleftharpoons CF_4 + C - 107.2$

(d) $C_2F_4 \rightleftharpoons CF_3 + CF - 107.9$

(e) $C_2F_4 \rightleftharpoons 2CF + F_2 - 301.4$

(f) $C_2F_4 \rightleftharpoons C_2F_2 + F_2 - 104.2$

(g) $CF \rightleftharpoons C + F - 114.4$

(h) $CF_2 \rightleftharpoons CF + F - 85.3$

(i) $CF_3 \rightleftharpoons CF + F_2 - 193.5$

(j) $CF_3 \rightleftharpoons CF_2 + F - 108.2$

(k) $CF_4 \rightleftharpoons CF_3 + F - 115.1$

(l) $CF_4 \rightleftharpoons CF_2 + F_2 - 186.5$

(m) $CF_4 \rightleftharpoons CF + F_2 + F - 308.6$

(n) $C_2F_2 \rightleftharpoons 2CF - 197.2$

(o) $C_2F_2 \rightleftharpoons CF_2 + C - 189.5$

(p) $C_2F_2 \rightleftharpoons 2C + F_2 - 389.2$

(q) $F_2 \rightleftharpoons 2F - 36.8$

On the basis of the energy requirements for the above reactions it appears that the existence of all species, i.e., C, F, CF, CF_2, CF_3, CF_4 and C_2F_2, are equally probable. If one considers the overall dissociation energy of $C_2F_4 \rightleftharpoons 2C + 4F$ a value of 467.8 kcal/mole is obtained. A molecular weight of 100g/mole leads to a total energy requirement of 4678 cal to completely dissociate one gram of the monomer. Hence, a total of .692 cal (2.9J) is required to completely dissociate the 0.148 mg of ablated TFE generated per discharge. It would therefore appear that a reasonable approximation to the chemical kinetics is to assume that the monomer is completely dissociated instantaneously upon being ablated because of the excessive energy being deposited into the resulting gas. This approximation is, however, contingent not only upon the energy being available but also upon the reaction rate being sufficiently high with respect to the discharge time to guarantee that the dissociation will proceed to completion. Not having the necessary data to compute the forward rates of the above reactions does not allow verification of this approximation. Moveover, the nonlinear way in which the energy is deposited into the ablated solid leads to the question as to whether or not sufficient energy per unit mass is available for complete dissociation at all times during the discharge. The experimental data accumulated throughout this study suggests that after the first

cycle of the discharge oscillation there probably is not sufficient energy being deposited into the ablating solid to completely dissociate the gaseous products but the high density and temperature near the surface of the solid propellant and the abundance of energy available for dissociation indicate that the assumption of a fully dissociated gas is probably valid at least for the first cycle of the discharge.

Ionization of the gas mixture 2C + 4F is considered next. The first four ionization levels for fluorine are 419.6, 1226.6, 2670.9 and 4682.7 kcal/mole. For carbon gas these are 430.2, 992.3, 2096.2, and 3583.1 kcal/mole. Thermal ionization is postulated as being the major mechanism for production of electrons. The corresponding rate equation for this process is

$$\dot{n}_i = \dot{n}_e = n_i n_e k_f - n_n k_r = -\dot{n}_n$$

where n_i, n_e and n_n are the number densities of ions, electrons, and neutrals; respectively. k_f is the forward reaction rate constant and k_r is the reverse reaction rate constant. In a static equilibrium situation the reverse and forward rates of reaction must be equal and one eliminates having to know one of the rate constants by solving for it in terms of the equilibrium constant k_p. The following is then obtained:

$$\dot{n}_i = k_f (n_i n_e - k_p n_n)$$

where k_p is given by the Saha equation

$$K_p = 4.828 \times 10^{15} G T_e^{\frac{3}{2}} \exp\left(- \frac{\epsilon_I}{kT_e} \right)$$

where G is the statistical weight (taken to be 1.5), ϵ_I is the ionization potential, T_e is the absolute temperature and K_p has the units cm^{-3}. With more than one neutral and ion species present, the above rate equation is written for each different species with n_i and n_n the number densities of the ion and neutral of that species only whereas n_e is the total number density of electrons. Typically, k_f will obey an Arrhenius formula

$$k_f = C T_e^{\omega} \exp\left(- \frac{\epsilon_I}{kT_e} \right)$$

where C and ω are constants. For neutrals of atomic species ω usually has the value $\frac{1}{2}$. The value of the constant C is only approximately determined by kinetic

theory and is usually adjusted to match known reaction rates by multiplying the value obtained from kinetic theory by a number called the "steric factor." The uncertainty in the value of C essentially makes it an unknown unless data is available which allows one to compute the proper value. No such data is available for ionization of carbon and very little is available for fluorine ionization. It hardly makes sense, therefore, to consider nonequilibrium ionization of each individually, thereby introducing two unknowns when one can approximate the true state of affairs by assigning a single forward rate to electron production from both neutral species and treat the 2C + 4F neutral gas mixture as a single background gas having an average molecular weight of 16.67. In doing so the problem is reduced to one of determining a single value of C which leads to the correct result. The implicit assumption is that the mole fractions of C and F remain the same throughout the calculation.

4.4 Numerical Integration Scheme

The computational technique to be used for solution of Equation (7) is a second order accurate, two-step explicit numerical integration scheme. The scheme has been applied successfully in the past for solution of conventional gas dynamics problems including discontinuous flows[19], flows containing finite rate chemical reactions[20], viscous, heat conducting flows[21], and radiative flows[22]. In all cases, this numerical technique has demonstrated extremely high accuracy when compared to available analytic solutions. The precise form of the scheme is given in Appendix B.

Since, to the best of our knowledge, this scheme has not been used previously to solve MHD problems, a linearized stability analysis was performed to determine the conditions on Δt and Δx or Δy required for stability of the calculations. The analysis consists of linearizing the finite difference approximation to Equation (3) so that a single equation relating W at $t + \Delta t$ to W at t is obtained and then substituting a Fourier component solution of the form $a(t) \exp(i\alpha x + By)$ for W (x, y, t). One then obtains a system of five simultaneous linear algebraic equations for $a(t + \Delta t)$ in terms of a(t). The matrix relating these two vectors is called the amplification matrix, and for Equation (3) this matrix is a function of the arguments $(\Delta t/\Delta x)$, $(\Delta t/\Delta y)$, $C_T \Delta t/\Delta x^2$, and $C_T \Delta t/\Delta y^2$; where C_T is any of the transport coefficients (i.e., $1/\sigma u$, ν, or K). To determine whether or not the scheme is stable in this linear sense, one searches for values of these quantities which lead to eigenvalues of the amplification matrix having a magnitude less than one over all space. For brevity, the details of this procedure are not presented here and only the results are discussed.

The finite difference scheme is linearly stable in the case of zero dissipation for all values of $\Delta t/\Delta x$ satisfying the relationship

$$\frac{\Delta t}{\Delta x} \leq \min_{\forall(x,y)} \left[\frac{.7}{|u|+c}, \frac{.7}{|v|+c} \right] \tag{8}$$

where the argument on the right hand side is evaluated at each point in the flow field at each level of time and the minimum value is used to compute all points at the next level of time.

This result is a logical extension of the results obtained when solving non-dissipative, two-dimensional unsteady ordinary fluid dynamics problems. In that case the characteristic wave speed c is the speed of sound. In a MHD flow, the speed c is the root mean square of the speed of sound and the Alfven speed $(B^2/\mu\rho)^{\frac{1}{2}}$. In the case of finite dissipation the results are also similar to those obtained for ordinary dissipative fluid dynamics problems. It is found that for values $C_T\ \Delta t/\Delta x^2$ greater than or equal to approximately 10 stability is obtained with $\Delta t/\Delta x$ given by Equation (8); and as the value of this parameter is made smaller, the value of $\Delta t/\Delta x$ required for stability becomes smaller than that given by Equation (4). A discussion of the reasons for this behavior is given in Ref. 21 where it is also concluded that to obtain the required spatial resolution of the flow field and retain second order accuracy of the timewise solution, the magnitude of the time-step must be the same or smaller than the smallest characteristic diffusion time.

5.0 RESULTS OF CALCULATIONS

The first calculations which were performed were done using the one-dimensional unsteady model with finite electrical conductivity the only dissipative mechanism. For reasons unknown at the time those calculations became unstable almost immediately. Considerable effort was exerted in varying the initial conditions to determine whether or not an inconsistent set of initial conditions was the cause of the instabilities. This proved not to be the case. After due consideration of this numerical problem it was determined that the actual reason for development of instability was an unfortunate choice of models. Namely, neglecting the displacement current term in Maxwell's equations had led to a set of MHD equations which were physically unrealistic in certain regions of the flow field. Precisely how the eroneous physical model and instabilbity are related is discussed below.

One of the approximations to Maxwell's equations which is normally made in treating MHD flows is to neglect displacement currents with respect to conduction currents. This approximation is usually a good one except at very low frequencies. Disregarding displacement currents has the secondary effect of eliminating pure electromagnetic wave propagation which, in most flow problems of interest, is not a significant effect. It turns out, however, that in a flow such as the one being analyzed during this program where the advancing plasma is interfaced with a true vacuum on its boundaries, the propagation of electromagnetic waves ahead of the plasma is important. At non-relativistic plasma velocities the effects of these waves on the overall solution to the problem can still be neglected but in a problem wherein the characteristic plasma wave speed can approach the speed of light the assumption of negligible displacement currents must be reevaluated. In the problem at hand this is the case because the basic mechanism associated with plasma acceleration is an expansion which converts both thermal and magnetic energy to kinetic energy. At the leading edge of this expansion (i.e., the vacuum/plasma contact surface) the plasma density must approach zero whereas the magnetic flux density may be finite. Thus, the characteristic wave speed (i.e., the Alfven speed) at the contact surface will approach infinity if the displacement current is neglected. What must physically happen is shown in Figure 19. The fast plasma waves will asymptote the principal electromagnetic waves and secondary electromagnetic waves will penetrate the plasma asymptoting the slow plasma waves. This will occur in a continuous fashion as the collision dominated (high density) plasma expands to a free molecule flow. In the original

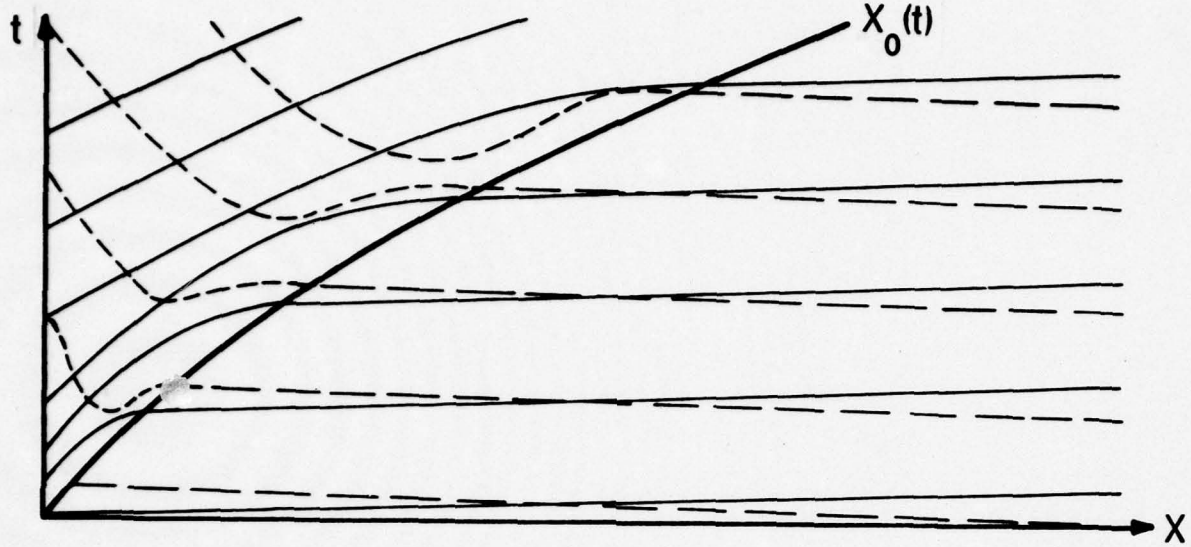


DIAGRAM NOT TO SCALE

—— PLASMA FRONT $X = X_0(t)$

—— PRINCIPAL CHARACTERISTICS

– – CROSS CHARACTERISTICS

$dx/dt = U + S = C$ FOR $X \geq X_0$

$dx/dt = U - S = -C$ FOR $X \geq X_0$

Figure 19. Typical Wave Propogation Diagram

FAIRCHILD
HILLER PUBLIC COMPANY

formulation of this problem neglecting displacement currents allowed the wave speed to become infinite rather than being limited to the speed of light and the instabilities encountered were simply a result of not being able to choose a value of $\Delta t/\Delta x$ smaller than was necessary to accommodate the physically unrealistic infinite wave speed.

Inclusion of the displacement current in the Biot-Savart Law introduces considerable additional complexity to the governing equations due to the appearance of additional terms in the Lorentz force ($\underline{J} \times \underline{B}$) and the power dissipation ($\underline{E} \cdot \underline{J}$). Elimination of $\overline{E}$ as a dependent variable via Ohm's Law and Faraday's Law further complicates matters. One finds, however, that certain reasonable approximations can be made which eliminate the majority of these additional terms. To illustrate this the one-dimensional unsteady equations will be considered.

The induction equation, obtained by differentiating Ohm's Law once with respect to X, and replacing $\partial E/\partial x$ by $-\partial B/\partial t$ becomes

$$B_t + (uB)_x = \frac{1}{\sigma\mu} \left(B_{xx} - \frac{1}{c^2} B_{tt}\right)$$

which differs from the original model by the last term. The Lorentz force takes the following form with displacement currents included:

$$\underline{J} \times \underline{B} = JB = -\frac{1}{2\mu} B_x^2 - \epsilon_o (uB^2)_t - \frac{1}{2} \epsilon_o (u^2 B^2)_x$$

$$- \frac{\epsilon_o B}{\mu\sigma} E_{xx} - \frac{1}{c^2} E_{tt} - u \left(B_{xx} - \frac{1}{c^2} B_{tt}\right)$$

Only the first term on the right hand side is obtained when displacement currents are not included. Finally, the power dissipation term becomes;

$$\underline{E} \cdot \underline{J} = EJ = \frac{1}{\sigma\mu^2} (BB_x)_x - \frac{1}{\mu} (uB^2)_x - \frac{1}{2\mu} B_t^2 - \frac{\epsilon_o}{2} E_t^2 + \frac{\epsilon_o}{\sigma\mu} (BE_t)_x$$

whereas only the first three terms appear when displacement currents are negligible. The first fact that becomes obvious upon looking at the additional terms is that the electric field appears explicitly as an added dependent variable which cannot be eliminated. Hence, Faraday's Law in differential form would be included in the list of equations to be solved to close the system. The second and more important observation is that the differential equations to be solved are second order in time

whereas the original (no displacement current) equations were first order in time. Fortunately, it is possible to simplify the resulting equations when the speed of the plasma is nonrelativistic. In order to make this approximation we note that within the plasma variations in time are of the same order as the product of velocity and variations in space. Mathematically this is written as

$$0\,(W_t) = 0\,(uW_x)$$

and, therefore, $0\,(W_{tt}) = 0\,(u^2 W_{xx})$

for any variable W. As a result of this it is seen that terms of the form W_{tt}/c^2 may be neglected as being small compared to W_{xx} because (u/c) is much less than one. It is also noted that the third term in the Lorentz force expression may be neglected in comparison to the first term for the same reason. The term proportional to $\epsilon_o B/\mu\sigma$ is negligible by comparison to the remaining terms for typical values of σ. Near the contact surface, however, σ can be relatively small but the term would vanish identically there since the wave equation for E and B will be automatically satisfied as one approaches the vacuum. Indeed, this is the limit of the MHD equations including displacement currents when σ approaches zero. Additional terms in the power dissipation term are systematically eliminated using the same arguments and the additional assumption that within the plasma the energy stored in the electric field (i.e., $\epsilon_o E^2/2$) is small compared to the total plasma energy. Thus, the momentum and energy equations which are valid approximations to the generalized MHD equations under the assumptions of nonrelativistic flow velocity, negligible electric field energy, and moderate to high electrical conductivity are

$$(\rho u + \epsilon_o u B^2)_t = -\,(p^* + \rho u^2)_x$$

$$E_t = -\left[u(E + p^*)\right]_x + \frac{1}{\mu^2}\left(\frac{B}{\sigma}\,B_x\right)_x$$

The induction and continuity equations remain unchanged as is the energy equation. Note, however, that the momentum equation includes an additional term which could not be neglected on the basis of any of these assumptions. Rewirting the left hand side of the momentum equation as follows:

$$(\rho u + \epsilon_o u B^2)_t = \left[\rho u \left(1 + \frac{B^2}{\rho \mu c^2}\right)\right]_t$$

it is immediately obvious that the additional term is simply proportional to the square of the ratio of the Alfven speed to the speed of light. Under conditions wherein the magnetic flux is large and the density low this term can have an appreciable effect on the solution even though all approximations made to the generalized MHD equations may be valid.

The procedure used in calculations performed subsequent to the above reformulation is as follows. The solution region is divided into two domains; between the ablation surface and the plasma leading edge wherein the MHD equations (including the modified momentum equation) are utilized, and between the leading edge and infinity, wherein the equations governing electromagnetic wave propagation are utilized. The location of the plasma leading edge not being a known function of time a priori, one must also compute its location. Based on the previous arguments a reasonable criterion which establishes the location of the plasma leading edge for all practical purposes is the condition

$$\frac{B^2_{LE}}{\rho_{LE}} \leq \frac{1}{\epsilon_o}$$

For values of B_{LE} which are typically on the order of one T, the above establishes a lower limit on the leading edge density of 2.8×10^{-11} kg/m^3. This value is clearly beyond the acceptable limits of continuum theory and one must necessarily be cautious concerning results in the neighborhood of the leading edge. The two solution regimes are "matched" at the leading edge by the boundary condition on B as determined in Section 4.1.2.

Calculations performed using the procedure described above allowed stable computation to proceed much farther forward in time than was possible originally. The separation of the initial arc and generation of a secondary standing arc were actually observed in the numerical solutions. Results of a typical run are presented in Figure 20 where B and J are plotted as a function of distance at four different times during the first quarter cycle. As postulated through analysis of the experimental data, what appears to be separation of the initial arc is actually a splitting of the arc

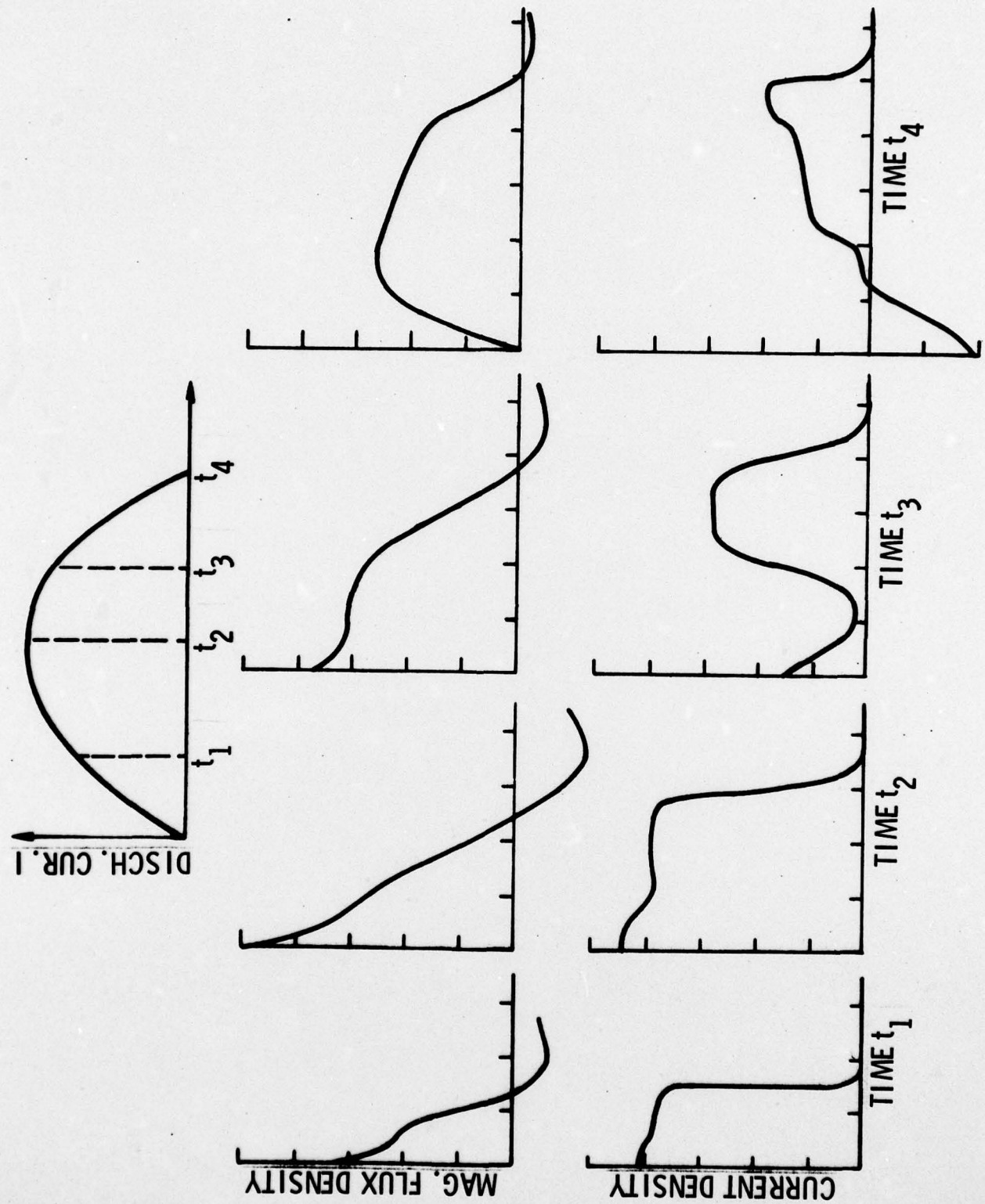


Figure 20. Computed Magnetic Flux and Current Density Distributions During the First Quarter Cycle

into two separate arcs carrying current in opposite directions. This occurs at the onset of reversal in the gradient of B at the ablation surface and has no relationship to the time at which the discharge current passes through zero. In fact, current is already flowing in the opposite direction at the ablation surface when discharge current reverses, eliminating the necessity for a "restrike" of the arc. The reversal in the gradient of B at the ablation surface is the result of two concurrent phenomena. First, as the discharge current passes through its maximum value and begins to decay so does the magnitude of B at the ablation surface. Second, the magnetic field energy being carried away from the ablator by the plasma is continually decreasing in the vicinity of the wall because of the continual conversion of this energy into kinetic energy via the MHD expansion process. It is apprent, however, that the characteristic time associated with the decrease in the value of B at the ablation surface is larger than the characteristic flow time in the vicinity of the surface. Hence, B decays more rapidly at the surface, the rate of decrease being dominated by the overall discharge circuit, than it does as a result of energy conversion near the surface (which is dominated by the local flow characteristics).

Numerical instability is encountered soon after arc splitting. The reason for the instability is directly associated with the degeneration into two separate arcs, which has the effect of producing a low density region between the standing and accelerating arc. The low density region between the two coexistent arcs is caused by amplification of the magnetic flux density between the arcs tending to push the standing arc against the ablator surface and push the accelerating arc away from the standing arc. This configuration of forces exists until the magnetic flux at the surface of the ablator becomes negative (approximately the same time the discharge current reverses), at which time the magnetic pressure gradient within the standing arc becomes favorable. During the period of time that this force configuration exists no mass can enter the region between the two arcs and extremely low densities exist between them. As soon as the Alfven speed between the arcs becomes larger than the speed of light the calculations again become unstable. Note that this problem was circumvented at the leading edge by limiting the upstream density to some small but finite value and computing the magnetic flux ahead of it using standard electromagnetic wave equations. With a similar region embedded within the computational flow field such a methodology is not as simple. Indeed, with undefined boundaries on both sides of the region the problem is quite unmanageable. Finally, after many

attempts at resolving this problem the authors were forced to concede and concentrate on resolution of the acceleration mechanics for the first quarter cycle only.

Uncertainties concerning appropriate values for plasma conductivity, scaling length and plasma density made the process of obtaining good quantitative agreement between the computed flow field and experimental data a tedious one. A process of trial and error coupled with analytical reasoning was undertaken during approximately the last year of this program with that objective. Those efforts were only moderately successful because of the number of parameters whose unknown values could encompass a considerable range. Hence, although an excellent qualitative picture of the acceleration mechanism was obtained no absolute quantitative agreement was generated.

6.0 CONCLUSIONS

The difficulties encountered in the numerical formulation of boundary conditions for the analytic model did not allow calculations to proceed much beyond the first quarter cycle of the capacitor discharge. Nevertheless, an excellent qualitative picture of the acceleration up until that time was obtained from the calculations and verified by the experimental data taken. Good quantitative agreement with the experimental data was not obtained because of the uncertainty in the values of several important parameters. Despite these deficiencies in the theoretical modeling certain conclusiions concerning plasma acceleration in ablative arcs can be made on the basis of what it was possible to accomplish.

The majority of the discharge energy is deposited into the plasma in the vicinity of the ablation surface. Energy is consumed there for the most part in dissociating, ionizing and heating the ablated mass and in creation of magnetic field. Plasma acceleration is then accomplished via an MHD expansion in which magnetic and, to some degree, thermal energy are converted to kinetic energy. The process may be visualized as being divided into two regions; an energy deposition region in the vicinity of the ablator, and an energy conversion region which is the MHD expansion fan. There is a continuous transition between these two regions until arc splitting occurs, a process which is the result of the distribution of forces as the discharge current begins to decay from its peak value. When this occurs a portion of the initial arc remains at the surface of the ablator and the remainder continues to accelerate. Mass is retained within the portion left standing at the ablator until the magnetic flux changes direction at the surface, at which time the standing arc also begins accelerating. The region between the two arcs has very low density because the force distribution does not allow for the flow of plasma therein. Upon reversal of the discharge current the above process appears to be duplicated with the second plasmoid being accelerated in much the same fashion as the first. As successive arcs are formed and accelerated there is less energy available to each and the ultimate velocity which each plasmoid reaches is therefore lower. The fact that less energy is available to each arc as the discharge progresses is offset somewhat by the fact that each successive plasmoid contains less mass, which maintains the energy/mass ratio of each at a high value. This particular observation points out a very basic difference between plasma acceleration of ablated mass products as opposed to acceleration of plasmas produced in gaseos injection type devices. That

is, in gaseous propellant devices the mass flow rate of gas into the acceleration channel is constant (being limited to sonic velocity at the injection orifice), whereas ablative plasma generation occurs at a rate determined by the discharge current. The rate of mass addition to the discharge channel at any given time is therefore more consistent with the amount of energy available to accelerate that mass in ablative plasma accelerators than in those using gaseous injection of propellant.

The qualitative understanding of the acceleration process which has been developed as a result of this program does not immediately yield information which will make it possible to design more efficient accelerators, but considerable insight into the plasma dynamics of such devices has been obtained and it is conceivable that further consideration of these results will assist in future development. Plans for the immediate future are directed at an examination of the plume emanating from millipound thruster systems using ablative plasma acceleration. An investigation of the plume via a pulsed Langmuir probe to be developed during that effort will be carried out and a Monte Carlo stochastic model will be used in attempting to describe the plume analytically.

7.0 REFERENCES

1. Guman, W.J. and Nathanson, D.M., "Pulsed Microthruster Propulsion System for Synchronous Orbit Satellite," J. Spacecraft and Rockets, Vol. 7, No. 4, Page 409, April 1970.

2. Vondra, R.J. and Thomassen, K.I., "A Flight Qualified Pulsed Electric Thruster for Satellite Control," AIAA Paper 73-1067, AIAA 10th October 1973.

3. Guman, W.J., and Williams, T.E., "Pulsed Plasma Microthruster for Synchronous Meteorological Satellite (SMS), AIAA Paper No. 73-1066, October 1973.

4. Guman, W.J., and Kowel, S.J., "Pulsed Plasma Propulsion System for TIP-II Satellite," 1975 JANNAF Propulsion Meeting, September 1975.

5. Palumbo, D.J., and Guman, W.J., "Propellant Side Feed-Short Pulsed Discharge Thruster Studies," NASA CR-112035, January 1972.

6. Palumbo, D.J., and Guman, W.J., "Pulsed Plasma Propulsion Technology," AFRPL-TR-73-79, Air Force Rocket Propulsion Laboratory, Edwards AFB, Calif., September 1973.

7. Palumbo, D.J., Begun, J., and Guman, W.J., "Pulsed Plasma Propulsion Technology," AFRPL-TR-74-50, Air Force Rocket Propulsion Laboratory, Edwards AFB, Calif.

8. Guman, W.J., "Designing Solid Propellant Pulsed Plasma Thrusters," AIAA Paper No. 75-410, March 1975.

9. Palumbo, D.J. and Begun, M., "Plasma Acceleration in Pulsed Ablative Discharges," AFOSR-TR-75-0618, Air Force Office of Scientific Research, Bolling AFB, D.C., March 1975.

10. Palumbo, D.J. and Begun, M., "Plasma Acceleration in Pulsed Ablative Discharges," AFOSR-TR-76-0738, Air Force Office of Scientific Research, Bolling AFB, D.C., March 1976.

11. Madorsky, S.L., Hart, V.E., Straus, S., and Sedlak, V.A., "Pyrolysis of Polytetrafluoroethylene and Hydrofluoroethylene Polymers in Vacuum," J. Res. Nat. Bur. Std. Vol. 51, pp 327-333, (1953).

12. Lewis, E. and Naylor, M., "Pyrolysis of Polytetrafluoroethylene," J. Am. Chem. Soc., Vol. 69, pp 1968-1970 (1947).

13. Anderson, H.C., "Pyrolysis of Polytetrafluoroethylene," Makromol. Chem., Vol. 51, pp 233-235 (1962).

14. Siegle, J.C. and Muua, L.T., "Pyrolysis of Poytetrafluoroethylene," 150th Nat. Mfg. of Am. Chem. Soc. (1956).

15. Straus, S. and Madorsky, S., "Pyrolysis of Some Polyvinyl Polymers at Temperatures to 1200°C," J. Res. Nat. Bur. Std., Vol. 66A, pp 401-406 (1962).

16. Duus, H.C., "Thermochemical Studies on Fluorocarbons," Ind. Eng. Chem. Vol. 47, pp 1445-1449 (1955).

17. Mathias, E. and Miller, G.H., "The Decomposition of Polytetrafluoroethylene in a Glow Discharge," J. Phys. Chem., Vol. 71, No. 8, pp 2671-2675 (1967).

18. Settlage, P.H. and Siegle, J.C., "Behavior of Teflon Fluorocarbon Resins at Elevated Temperatures," Symp. on Fluorocarbon Chem. pp. 73-81.

19. Bohachevsky, T.O., and Rubin, E.L., "Numerical Calculation of Discontinuous Flows," AIAA J., Vol. 4.

20. Palumbo, D.J., and Rubin, E.L., "Numerical Solution to Chemical Relaxation Behind Normal Shock Waves in Air," Poly. Inst. of N.Y., PIBAL Report No. 68-18 (1968).

21. Palumbo, D.J. and Rubin, E.L., "Numerical Solution to the Compressible Navier-Stokes Equations in Two-Dimensions," J. Comp. Phys., Vol. 9, No. 3, p. 466, 1972.

22. Rubin, E.L., and Khosla, P., "Discontinuous Flows with Radiation," Math. Phys., Vol. 21, p. 962, 1970.

APPENDIX A

GOVERNING EQUATIONS - VECTOR DEFINITIONS

Nomenclature:

ρ	=	Total plasma density
ρ_α	=	Density of species α
u	=	x-component of velocity
v	=	y-component of velocity
E_α	=	Energy density of species α
E	=	Total energy density
B	=	Magnetic flux density
p_α	=	Partial pressure of species α
p^*_α	=	$p_\alpha + B^2/2$
V_1	=	$2(2u_x - v_y)/3$
V_2	=	$u_y + v_x$
V_3	=	$2(2v_y - u_x)/3$
η	=	Viscosity coefficient
σ	=	Electrical conductivity
K	=	Thermal conductivity of species
e_α	=	Specific internal energy of species α
$\nu_{\alpha\beta}$	=	Collision frequency between α and β species
I_p	=	Ionization potential (J/kg)
T_α	=	Temperature of species α
m_α	=	Mass of species α
$\dot{n}_i$	=	Ion production rate

Dependent Variables Vector:

$$W = \begin{bmatrix} \rho \\ \rho_i \\ \rho u \\ \rho v \\ E_e \\ E_i \\ B \end{bmatrix}$$

Advection Vectors:

$$f = \begin{bmatrix} \rho u \\ \rho_i u \\ p^* + \rho u^2 \\ \rho uv \\ u(E_e + p_e^*) \\ u(E_i + p_i) \\ uB \end{bmatrix} \qquad g = \begin{bmatrix} \rho v \\ \rho_i v \\ \rho uv \\ p^* + \rho v^2 \\ v(E_e + p_e^*) \\ v(E_i + p_i) \\ vB \end{bmatrix}$$

Dissipation Vectors:

$$F = \begin{bmatrix} 0 \\ 0 \\ \eta V_1 \\ \eta V_2 \\ K_e T_{e_x} + \frac{1}{\sigma\mu^2} B B_x \\ \eta(uV_1 + vV_2) + K_i T_{i_x} \\ \frac{1}{\sigma\mu} B_x \end{bmatrix} \qquad G = \begin{bmatrix} 0 \\ 0 \\ \eta V_2 \\ \eta V_3 \\ K_e T_{e_y} + \frac{1}{\sigma\mu^2} B B_y \\ \eta(uV_2 + vV_3) + K_i T_{i_x} \\ \frac{1}{\sigma\mu} B_y \end{bmatrix}$$

Source Vector:

$$S = \begin{bmatrix} 0 \\ m_i \dot{n}_i \\ 0 \\ 0 \\ -\rho_e (e_e - e_i)(\nu_{ei} + \nu_{en}) \\ \rho_i \nu_{ei} (e_e - e_i) \\ 0 \end{bmatrix}$$

Algebraic Relationships:

$$p_\alpha = \rho_\alpha \frac{k}{m_\alpha} T_\alpha$$

$$\rho_e = \frac{m_e}{m_i} \rho_i$$

$$e_e = \frac{3k}{2m_e} T_e = (E_e/\rho_e) - \frac{1}{2} q^2 - (B^2/2\mu)$$

$$e_i = \frac{3k}{2m_i} T_i = (E_i/\rho_i) - \frac{1}{2} q^2$$

$$q^2 = u^2 + v^2$$

APPENDIX B
FINITE DIFFERENCE SCHEME

$$W^{k+1}_{n,m} = W^{k}_{n,m} - \tfrac{1}{2}\lambda_x\left[\tfrac{1}{2}\left(f^{k}_{n+1,m} - f^{k}_{n-1,m}\right) + \bar{f}^{k+1}_{n+\frac{1}{2},m} - \bar{f}^{k+1}_{n-\frac{1}{2},m}\right]$$
$$- \tfrac{1}{2}\lambda_y\left[\tfrac{1}{2}\left(g^{k}_{n,m+1} - g^{k}_{n,m-1}\right) + \bar{g}^{k+1}_{n,m+\frac{1}{2}} - \bar{g}^{k+1}_{n,m-\frac{1}{2}}\right]$$
$$+ \tfrac{1}{2}\lambda_x\left[F^{k}_{n+1,m} - F^{k}_{n-1,m}\right] + \tfrac{1}{2}\lambda_y\left[G^{k}_{n,m+1} - G^{k}_{n,m-1}\right]$$

$$\lambda_x \equiv \frac{\Delta t}{\Delta x} \qquad \lambda_y \equiv \frac{\Delta t}{\Delta y}$$

$$W^{k}_{n,m} \equiv W(x + n\Delta x,\ y + m\Delta y,\ t + k\Delta t)$$

$$\bar{f}^{k+1}_{n\pm\frac{1}{2},m} \equiv f\left(\bar{W}^{k+1}_{n\pm\frac{1}{2},m}\right)$$

$$\bar{g}^{k+1}_{n,m\pm\frac{1}{2}} \equiv g\left(\bar{W}^{k+1}_{n,m\pm\frac{1}{2}}\right)$$

$$\bar{W}^{k+1}_{n\pm\frac{1}{2},m} = \tfrac{1}{2}\left(W^{k}_{n\pm1,m} + W^{k}_{n,m}\right) \mp \lambda_x\left(f^{k}_{n\pm1,m} - f^{k}_{n,m}\right) - \lambda_y\left(g^{k}_{n\pm\frac{1}{2},m+\frac{1}{2}} - g^{k}_{n\pm\frac{1}{2},m-\frac{1}{2}}\right)$$
$$\pm \lambda_x\left(F^{k}_{n\pm1,m} - F^{k}_{n,m}\right) + \lambda_y\left(G^{k}_{n\pm\frac{1}{2},m+\frac{1}{2}} - G^{k}_{n\pm\frac{1}{2},m-\frac{1}{2}}\right)$$

$$\bar{W}^{k+1}_{n,m\pm\frac{1}{2}} = \tfrac{1}{2}\left(W^{k}_{n,m\pm1} + W^{k}_{n,m}\right) - \lambda_x\left(f^{k}_{n+\frac{1}{2},m\pm\frac{1}{2}} - f^{k}_{n-\frac{1}{2},m\pm\frac{1}{2}}\right) \mp \left(g^{k}_{n,m\pm1} - g^{k}_{n,m}\right)$$
$$+ \lambda_x\left(F^{k}_{n+\frac{1}{2},m\pm\frac{1}{2}} - F^{k}_{n-\frac{1}{2},m\pm\frac{1}{2}}\right) \pm \left(G^{k}_{n,m\pm1} - G^{k}_{n,m}\right)$$

$$g^{k}_{n\pm\frac{1}{2},m\pm\frac{1}{2}} \equiv g\left[\tfrac{1}{4}\left(W^{k}_{n\pm1,m\pm1} + W^{k}_{n\pm1,m} + W^{k}_{n,m\pm1} + W^{k}_{n,m}\right)\right]$$

$$f^{k}_{n\pm\frac{1}{2},m\pm\frac{1}{2}} \equiv f\left[\tfrac{1}{4}\left(W^{k}_{n\pm1,m\pm1} + W^{k}_{n\pm1,m} + W^{k}_{n,m\pm1} + W^{k}_{n,m}\right)\right]$$

$$\left(W_x\right)^{k}_{n,m} = \frac{1}{2\Delta x}\left(W^{k}_{n+1,m} - W^{k}_{n-1,m}\right) \quad ; \quad \left(W_y\right)^{k}_{n,m} \equiv \frac{1}{2\Delta y}\left(W^{k}_{n,m+1} - W^{k}_{n,m-1}\right)$$

$$\left(W_x\right)^{k}_{n\pm\frac{1}{2},m\pm\frac{1}{2}} = \frac{\pm1}{2\Delta x}\left(W^{k}_{n\pm1,m} - W^{k}_{n,m} + W^{k}_{n\pm1,m\pm1} - W^{k}_{n,m\pm1}\right)$$

$$\left(W_y\right)^{k}_{n\pm\frac{1}{2},m\pm\frac{1}{2}} = \frac{\pm1}{2\Delta y}\left(W^{k}_{n,m\pm1} - W^{k}_{n,m} + W^{k}_{n\pm1,m\pm1} - W^{k}_{n\pm1,m}\right)$$

REPORT DOCUMENTATION PAGE

READ INSTRUCTIONS BEFORE COMPLETING FORM

1. REPORT NUMBER: AFOSR-TR-77-0623	2. GOVT ACCESSION NO.
3. RECIPIENT'S CATALOG NUMBER	
4. TITLE (and Subtitle): PLASMA ACCELERATION IN PULSED ABLATIVE ARC DISCHARGES.	5. TYPE OF REPORT & PERIOD COVERED: FINAL Rept. 15 March 1974 - 31 March 1977
	6. PERFORMING ORG. REPORT NUMBER
7. AUTHOR(s): DOMINIC J. PALUMBO, MARTIN BEGUN	8. CONTRACT OR GRANT NUMBER(s): F44620-74-C-0055
9. PERFORMING ORGANIZATION NAME AND ADDRESS: FAIRCHILD REPUBLIC COMPANY, FAIRCHILD INDUSTRIES, INC, FARMINGDALE, N Y 11735	10. PROGRAM ELEMENT, PROJECT, TASK AREA & WORK UNIT NUMBERS: 9782-02, 61102F
11. CONTROLLING OFFICE NAME AND ADDRESS: AIR FORCE OFFICE OF SCIENTIFIC RESEARCH/NA, BLDG 410, BOLLING AIR FORCE BASE, D C 20332	12. REPORT DATE: 1977
	13. NUMBER OF PAGES: 72
14. MONITORING AGENCY NAME & ADDRESS (if different from Controlling Office): 75 p.	15. SECURITY CLASS. (of this report): UNCLASSIFIED
	15a. DECLASSIFICATION/DOWNGRADING SCHEDULE

16. DISTRIBUTION STATEMENT (of this Report)

Approved for public release; distribution unlimited.

17. DISTRIBUTION STATEMENT (of the abstract entered in Block 20, if different from Report)

9782 02

18. SUPPLEMENTARY NOTES

19. KEY WORDS (Continue on reverse side if necessary and identify by block number)

PLASMA DYNAMICS
MAGNETO HYDRODYNAMICS
NUMERICAL TECHNIQUES
ABLATION
MATHEMATICS
PLASMA DIAGNOSTICS
PULSED DISCHARGES

20. ABSTRACT (Continue on reverse side if necessary and identify by block number)

This program was an effort to describe and understand plasma acceleration processes in pulsed ablative plasma accelerators using a continuum MHD approach as the basis for analytic modeling. Concurrent with analytic modeling, an experimental diagnostic effort was ~~also~~ performed so that calculated results could be compared to the measured parameters for * ~~evaluation~~ of the applicability ~~and accuracy~~ of the model. Diagnostic measurements ~~performed~~ included magnetic flux density using small coil probes, current distribution using a Rogowski coil, plasma front location and velocity using time of arrival probes, high speed

* Verification

photography using a high speed framing camera, and electron number density and temperature using Langmuir probes. Data was recorded on a digital memory oscilloscope, having appropriate frequency response. An unsteady two-dimensional model of the plasma motion including the dissipative effects of finite plasma conductivity, viscosity, and thermal conductance was postulated. The model included direct coupling of the external capacitor discharge circuit to the plasma via the time variant plasma resistance and inductance. A second order accurate two-step explicit numerical integration scheme was used to solve the resulting seven simultaneous parabolic partial differential equations and a second order Runge-Kutta technique was used to solve the two simultaneous second order ordinary differential equations for discharge current and potential. Ablated (depolymerized) solid propellant appears to be dissociated and ionized very quickly with respect to the duration of the discharge. Acceleration of the resultant plasma is dominated by expansion of the high density gaseous products near the surface of the ablator, transforming magnetic and thermal energy into kinetic energy. This process appears to be repeated during each quarter cycle of the oscillatory discharge as separate plasma bunches are generated. The process whereby these separate plasmoids are produced has been termed "arc splitting" and is the result of a force distribution within the arc which is dominated by Lorentz forces and the ratio of characteristic flow time to characteristic discharge time. The arc splitting process was observed numerically, although quantitative agreement with the experimental data was only margional because of the number of unknown independent parameters. The condition of large Alfven speed near the leading edge of the expansion required a unique modification to the MHD equations to insure stability of the calculation. Future work will have the objective of describing the plume emanating from pulsed ablative accelerators.